Photoproduction of pion pairs from calcium nuclei

PhD thesis

Frederic Bloch

Department of Physics and Astronomy
University of Basel, Switzerland
Klingelbergstrasse 82
CH-4056 Basel (Switzerland)

Contents

Chapter 1

Introduction

1.1 What physics?

The last Nobel Price (2004) has been given to David J. Gross, H. David Politzer and Frank Wilczek for "the discovery of asymptotic freedom in the theory of strong interaction" [1]. This is the characteristic feature of the strong interaction within the four forces of the standard model. The interaction of particles carrying color (quarks and gluons) described in QCD (quantum chromo dynamics) is stronger than the other interactions at the scale we meet it in nature (energy of the order of the nucleons mass). But when the distance between interacting particles gets smaller (i.e. energy larger) the strength of the interaction decreases, and the quarks become free at very short distances. This increase of the strong interaction with increasing distance makes it impossible to isolate a single quark and makes the quarks exist only in the form of hadrons (baryons made of 3 quarks or mesons made of one quark and one anti-quark).

The weakness of the strong interaction at large energy (small distances) allows the same kind of perturbative treatment as the very successful one developed in QED (quantum electro dynamics) by Feynman and others for the electromagnetic interaction. The prediction precision is there only limited by computing power.

Developing the interaction in power of the strong coupling constant is possible at very large energy (like hadron collisions at a few 100 GeV) but is not possible when this coupling constant is close to unity as it is the case at energies of the order of the nucleons or its resonances mass (a few GeV).

Behavior of this interaction at "usual energy" has then to be understood via other methods and many experiments are needed to gather informations about this physics (e.g. to understand the resonance spectrum of the nucleons)

1.2 Basics on chiral symmetry restoration

Chiral symmetry is an essential feature of the strong interaction. It is a symmetry of QCD in the limit of vanishing quark masses.
If quarks would be massless, they would move with the speed of light, and so in respect to any frame as says the relativity. Then a left (resp. right) handed particle would always be left (resp. right) handed. Left handed and right handed particles then "belong to two different worlds". But as soon as the quark has a mass, one can make up a frame moving "faster" than it. Then in this frame, a right handed particle becomes left handed (as the spin direction remains the same but the momentum of the particle points in the opposite direction). The left handed and the right handed worlds get mixed. The chiral symmetry exists in this massless limit of the quarks (called the chiral limit). It is almost the case for the quarks u and d at the typical hadronic scale of 1 GeV. But due to the few MeV mass of the quarks (5-10 MeV), the symmetry suffers from a small explicit breaking and is not perfect.
In addition to this tiny explicit breaking, the chiral symmetry is spontaneously broken as the QCD ground state (the vacuum) does not have the symmetry. The vacuum is far from being empty but is filled with quark/anti-quark pairs (called chiral condensate) that do not have the symmetry.
The non-invariance of the vacuum with respect to the three axial transformations requires existence of the three massless Goldstone bosons, which should be pseudo-scalars and form an isospin triplet (Goldstone bosons are massless particles introduced any time a continuous symmetry is spontaneously broken [5]). They are easily identified with pions as the pion mass is remarkably small compared to the other hadrons. The nonzero mass of pions is entirely due to the explicit chiral symmetry breaking by the small masses of the u and d quarks. Gell-Mann, Oaks, Rennes relation [6] gives the squares of the pion mass

$$m_\pi^2 = -\frac{1}{f_\pi^2}\frac{m_u + m_d}{2}(\langle \mathrm{u\bar{u}} \rangle + \langle \mathrm{d\bar{d}} \rangle) + O(m_{u,d}^2) \tag{1.1}$$

where f_π is the pion decay constant (f_π = 93 MeV).
Chiral symmetry implies parity doublets. For every baryon with the given quantum numbers and parity, there must exist another baryon with the same quantum numbers but opposite parity and which should have the same mass. This feature is not observed for the low lying states in hadron spectra, this is because the continuous chiral symmetry of the QCD Lagrangian is spontaneously (dynamically) broken in the vacuum. For example:

- $\mathrm{m}(\rho) << \mathrm{m}(\mathrm{a}_1)$ $\mathrm{J}^\pi=1^-,1^+$
- $\mathrm{m}(\pi) << \mathrm{m}(\sigma)$ $\mathrm{J}^\pi=0^-,0^+$
- $\mathrm{m}(\mathrm{N}(938)) << \mathrm{m}(\mathrm{N}^*(1535))$ $\mathrm{J}^\pi=1/2^+,1/2^-$

Actually, the number of massless Goldstone bosons is n_f^2-1 with n_f, the number of massless quarks (which is a subjective choice). If one considers that u and d quarks are massless, this introduces 3 massless bosons (the 3 pions). One can also consider that the strange quark is also massless compared to the three heavier quarks. Then it introduces 8 Goldstone bosons (π, K and η). The Goldstone bosons are more far from beeing massless in this case as the massless condition of the quarks is less exact.

The leading term of the Gell-Mann, Oaks, Rennes relation carries both the explicit breaking of the chiral symmetry (the quarks mass) and the spontaneous breaking (the chiral condensates $\langle q\bar{q}\rangle$). The chiral condensate expectation value depends on the density and the temperature. $\langle\bar{q}q\rangle$ at finite baryon density (ρ) obeys an exact theorem in QCD [2, 3, 4]:

$$\frac{\langle\bar{q}q\rangle}{\langle\bar{q}q\rangle_0} = 1 - \frac{\rho}{f_\pi^2 m_\pi^2}\left[\Sigma_{\pi N} + m\frac{d}{dm}\left(\frac{E(\rho)}{A}\right)\right], \tag{1.2}$$

where $\Sigma_{\pi N} = 45 \pm 10$ MeV is the pion-nucleon sigma term and $E(\rho)/A$ is the nuclear binding energy per particle with m being the current quark mass. $\langle\bar{q}q\rangle_0 \simeq -(225 \text{ MeV})^3$ represents the chiral condensate in the vacuum. The density dependence of (1.2) induces a reduction of almost 35 % of $\langle\bar{q}q\rangle$ already at the nuclear matter density $\rho_0 = 0.17\text{fm}^{-3}$. Fig 1.1 show the temperature and density dependence of chiral condensate in the Nambu, Jona-Lasinio model [8].

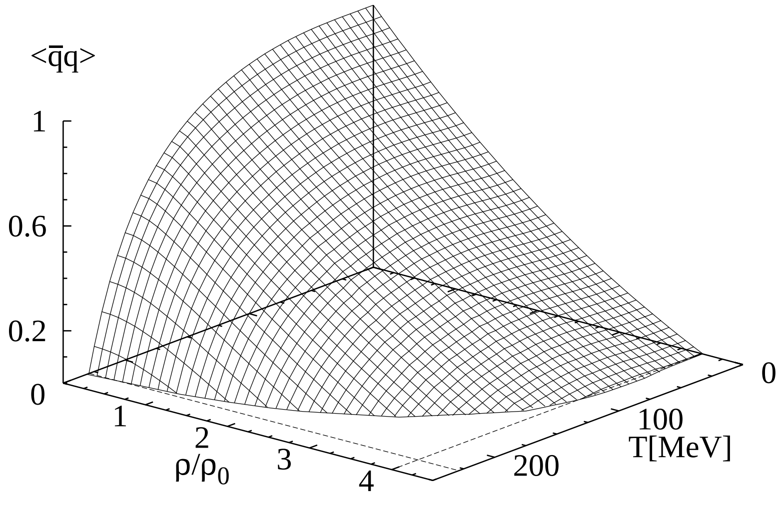

Figure 1.1: *temperature and density dependence of chiral condensate. (Nambu, Jona-Lasinio model)*

As the chiral condensates are responsible for the spontaneous breaking of chiral symmetry, a decrease of the expectation value of these condensates induces a partial restoration of this symmetry at large density. And then, the degeneracy of the parity doublets should be partly recovered with increasing density.

The effect of in-medium properties of the hadrons has been developed by Brown and Rho in [7] with the Brown-Rho scaling

$$\frac{m^*_{\sigma,\rho,\omega}}{m_{\sigma,\rho,\omega}} \approx \frac{m^*_N}{m_N} \approx \frac{f^*_\pi}{f_\pi} \tag{1.3}$$

with m^*, the in-medium mass of the corresponding hadron.
Predictions from QCD sum rules define the in medium σ and ρ meson mass as

$$m^*_{\sigma,\rho} \approx m_{\sigma,\rho}(1 - \alpha_{\sigma,\rho}\frac{\rho_N}{\rho_o}) \tag{1.4}$$

with $\alpha \approx 0.2$.
The σ-meson mass is predicted in the NJL model to decrease with increasing density and to be degenerate with the pion mass (its chiral partner) at some times the normal nuclear density [10] (see fig. 1.2).

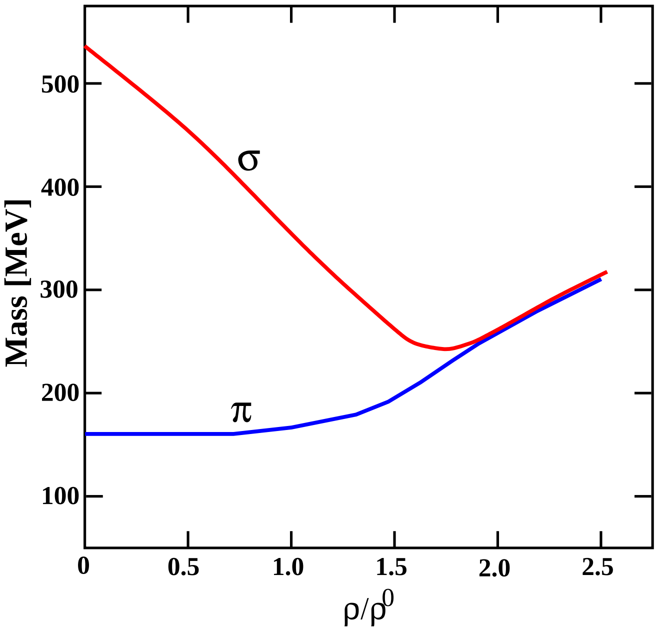

Figure 1.2: *σ mass in Nambu, Jona-Lasinio model as a function of density. ρ^0 is the normal nuclear density. If the density is large enough, chiral symmetry is restored and the degeneracy of the mass of the chiral partner (here the pion and the σ-meson) gets restored too.*

Such an effect could be accessible to our experiment via the $2\pi^o$ decay of the σ-meson. The mass of the pion pairs can be measured and compared for different targets (i.e. different average density). If a shift of the 2π mass distribution in the$\pi^o\pi^o$ channel is measured and is due to the above-discussed effects, it would not be visible in a non-zero isospin channel such as $\pi^o\pi^\pm$ (as the σ-meson is an isoscalar I=0 particle). Both channels have to be studied together and the target mass dependence compared.

Unfortunately this measurement meets an additional problem as in-medium $\pi\pi$ interaction can cause similar effects (see fig. 1.3). Even with the restoration parameter set to zero (α=0), an effect on the $\pi\pi$ mass is expected produced by the interaction of the two pions[9].

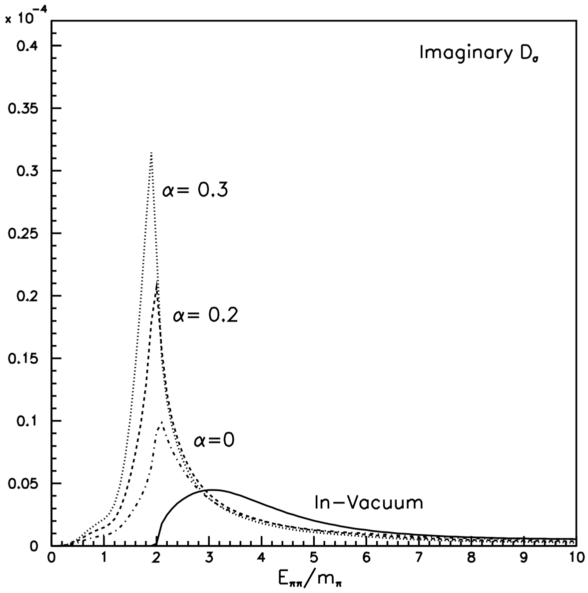

Figure 1.3: *Results for the imaginary part of the in-medium σ-meson propagator. Except for the vacuum case (full line curve) the remaining in-medium curves are computed at normal nuclear matter density. The dashed-dotted curve is for α=0, dashed for α=0.2 and the dotted for α=0.3.*

Motivating results have been obtained by the CHAOS collaboration [11, 12, 13, 14] in the isospin zero $\pi^+\pi^-$ channel compared to a non-zero isospin channel $\pi^+\pi^+$ (see fig. 1.4). The $\pi^+\pi^-$ mass distribution show more strength at low mass for heavy target (large nuclear density) like calcium or lead than for lighter targets like the proton target. The $\pi^+\pi^+$ distributions do not show the same kind of nuclear mass dependency. An acceptance hole of the spectrometer produced the peak/hole structure of the distributions and makes uneasy the comparison.

A similar effect was found by the Crystall Ball collaboration [15] in the $\pi^o\pi^o$ channel with a pion-induced experiment.

First results in $\pi^o\pi^o$ photoproduction from the TAPS colaboration have been published and discussed in [16, 17]. Contrarily to the CHAOS or Crystal Ball experiments, a photon beam was used. Pion beams, due to the strong initial state interactions, can only scan the surface of the nuclei. Electromagnetic probes

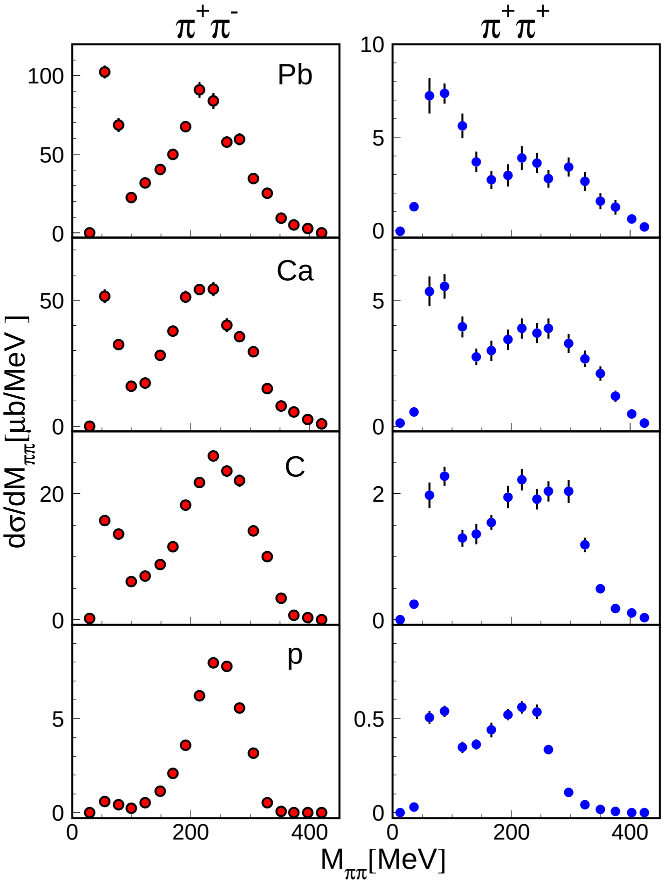

Figure 1.4: *Invariant mass distributions (diamonds) for* $\pi^+ \rightarrow \pi^+ \pi^-$ *and* $\pi^+ \rightarrow \pi^+ \pi^+$ *reactions on* ^2H, ^{12}C, ^{40}Ca *and* ^{208}Pb *(CHAOS collaboration)*

illumate the complete nucleus and lead to a larger effective density.

1.3 nucleons resonances

The nucleons (proton and neutron) are -with the electrons- the constituents of the matter. As they are a composite system made of quarks, they can be excited into resonances e.g. via electromagnetic interaction with real photons (photo-production) or virtual ones (electro-production). A level scheme of the low lying resonances is shown in figure 1.5. Resonances with isospin I=3/2 are usually called Δ-resonances, resonances with isospin I=1/2 are called N*-states. These states are defined by their mass and quantum numbers like isospin or parity. All these properties are summarized for the lighter resonances in table 1.1.

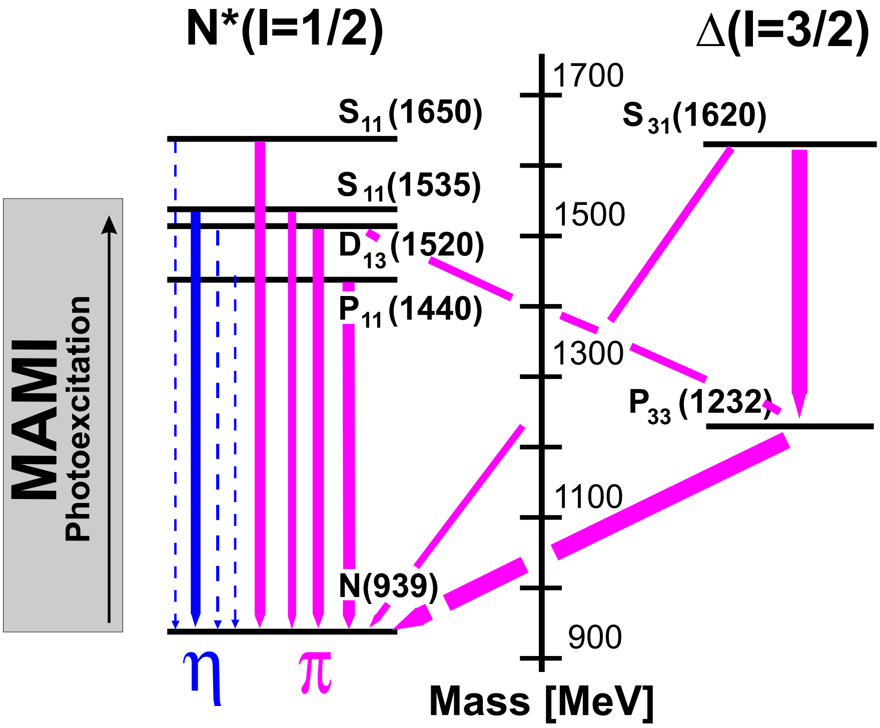

Figure 1.5: *Decay scheme of the low lying nucleon resonances. Arrows indicate meson decays of these states.*

The nucleon resonances can decay down to the ground state of the nucleon via strong interaction by the emission of mesons (like the π-meson or the η-meson). These decays are represented with arrows in fig. 1.5. As strong interaction is mainly responsible of the decay of the nucleon resonances, their life time is very short (typically 10^{-23}s). That induces a large width of 100 to 300 MeV.

The low lying resonances of the nucleon can be seen in a simple constituent quark model as a combination of spin flip of single quark and an orbital excitation of one of the three valence quarks in an harmonic oscillator potential (see figure 1.6). For instance, the Δ resonance is well understood by the flip of the spin of a single

Table 1.1: *Lowest lying N* and Δ resonances with their decay modes. In bold the modes that can contribute to the $\pi^o\pi^o$ or to the $\pi^o\pi^\pm$ channel. Data from [50].*

resonance (mass in MeV)	**width**	**I**	**J^P**	**decay modes**	
Δ resonances					
P_{33}(1232)	120 MeV	$\frac{3}{2}$	$\frac{3}{2}^+$	Nπ	>99%
				Nγ	<1%
P_{33}(1600)	350 MeV	$\frac{3}{2}$	$\frac{3}{2}^+$	**Δπ**	**40-70%**
				Nρ	**<25%**
				P_{11}(1440)π	**10-35%**
				Nπ	10-25%
S_{31}(1620)	150 MeV	$\frac{3}{2}$	$\frac{1}{2}^-$	**Δπ**	**30-60%**
				Nρ	**20-30%**
				Nπ	7-25%
N* resonances					
P_{11}(1440)	350 MeV	$\frac{1}{2}$	$\frac{1}{2}^+$	Nπ	60-70%
				Δπ	**20-30%**
				Nρ	**<8%**
				N$(\pi\pi)^{I=0}_{s-wave}$	**5-10%**
D_{13}(1520)	120 MeV	$\frac{1}{2}$	$\frac{3}{2}^-$	Nπ	50-60%
				Δπ	**15-25%**
				Nρ	**15-25%**
				N$(\pi\pi)^{I=0}_{s-wave}$	**<8%**
S_{11}(1535)	150 MeV	$\frac{1}{2}$	$\frac{1}{2}^-$	Nπ	35-55%
				Nη	35-55%
				P_{11}(1440)π	**<7%**
				Nρ	**<4%**
				N$(\pi\pi)^{I=0}_{s-wave}$	**<3%**
				Δπ	**<1%**

constituent quark of the nucleon. The notation of the resonances is made of a capital letter showing the relative angular momentum between the nucleon and the decay mesons. The usual convention is used (S for l=0; P for l=1; D for l=3). The two numbers represent 2×I and 2×J. Usually the mass of the resonance is given in brackets. The lighter resonance (called Δ resonance) is then named by P_{33}(1232). The three other resonances accessible with the available energy of the present work are P_{11}(1440), D_{13}(1520) and S_{11}(1535).

For more informations, photoproduction of mesons from free nucleons is discussed in detail in [18].

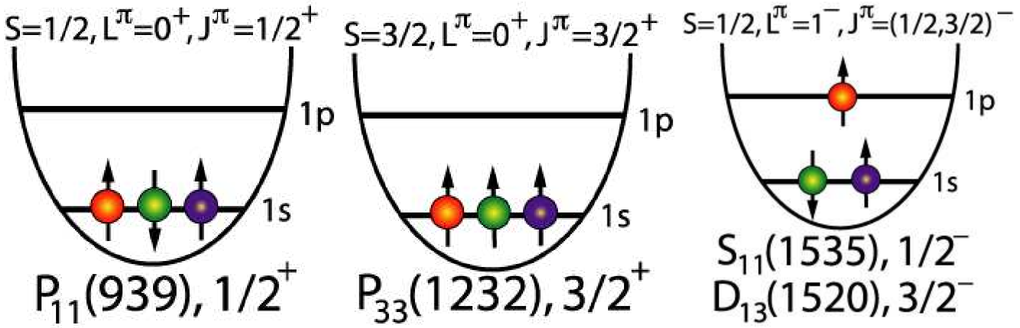

Figure 1.6: *Simple view of the low lying resonances of the nucleon in the constituent quark model.*

1.4 Second resonance region and $\pi\pi$ production

Results presented in this work have been measured in experiments that took place at the MAMI accelerator producing photons up to 882 MeV. This available energy can excite the nucleons in the $\Delta(1232)$ and the three lightest N^* resonances. These resonances are $P_{11}(1440)$, $D_{13}(1520)$ and $S_{11}(1535)$. They are called "the second resonance region" (the first one beeing only the $\Delta(1232)$).

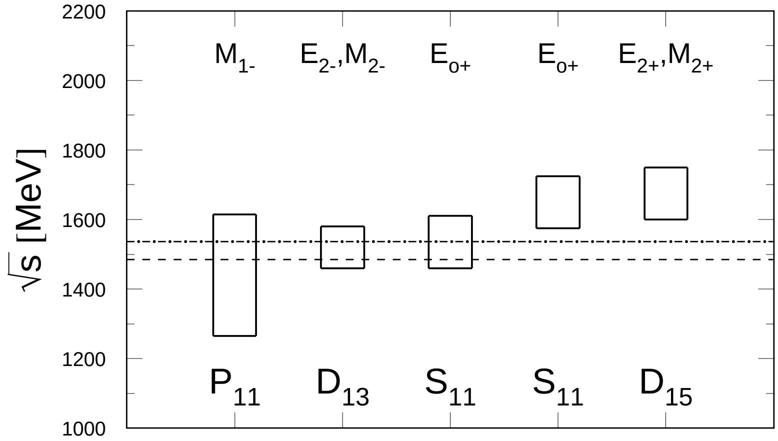

Figure 1.7: *Position and widths [35] of the low lying isospin 1/2 resonances. The dashed-dotted line the maximum tagged photon energy available at the MAMI accelerator. The multipoles corresponding to the excitation of the resonances are indicated on top of the figure.*

The large width combined to the close masses of the resonances induces an overlapping of the states of the second resonance region (see figure 1.7). This makes it non trivial to study an individual resonance (except in the particular case if they have exclusive decay channel like the $S_{11}(1535)$ with the $N\eta$ decay, see tab. 1.1 and [19, 20]).

The excitation function of total photoabsorption on the nucleon shows a large bump structure coming from the photons of 200 to 400 MeV exciting the Δ-resonance and another broad structure at high energy (photons of 500 to 900 MeV) corresponding to the 3 N*-states of the second resonance region. Many heavier resonances exist but they are not accessible to the energy available in this experiment.

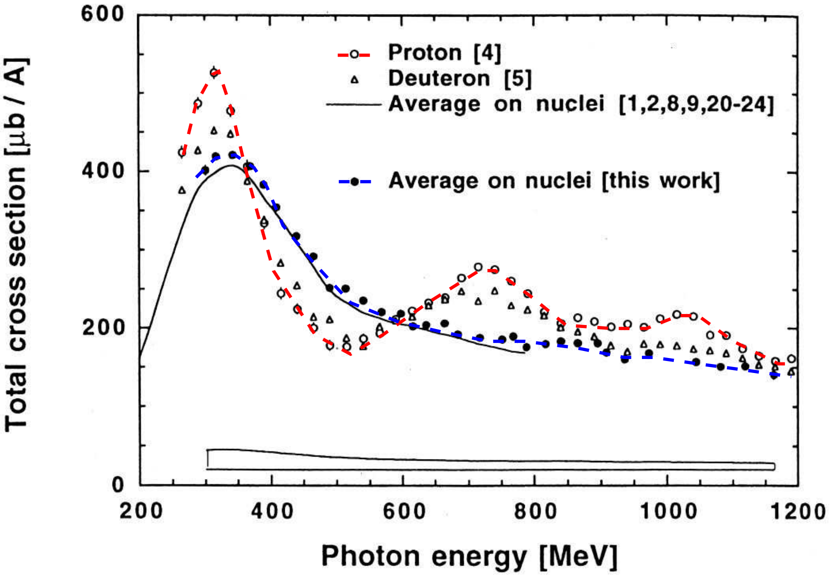

Figure 1.8: *Total photoabsorption on the proton and nuclei per nucleon. The second resonance region bump vanishes for nucleons [38].*

The peak structure of the total photoabsorbtion on the free proton in the second resonance region is not visible in total photoabsorbtion on nuclei (fig 1.8) [36, 37, 38]. The nuclear cross sections are almost identical when scaled by the atomic mass number from ^{7}Li to ^{238}U. This is expected since in total photoabsorption in contrast to individual reaction channels, no final state interaction effects can reduce the cross section, so that each additional nucleon gives the same contribution. The average of these cross sections on nuclei is represented as the "universal curve" and shows a depletion of the resonance structure in the second resonance region. Many effects are candidates to explain such important in-medium modification.

The most simple one is a broadening of the excitation functions due to Fermi motion of the bound nucleons. Also additional decay channels e.g. from NN* →NN collisions contribute to the broadening, while the Pauli blocking of final states counter acts and reduces the width of the resonances.

Total photoabsorption alone will not allow to study individual resonance contributions to nuclear cross sections and therefore during the last few years attempts have been made to measure exclusive reaction channels [21, 22].

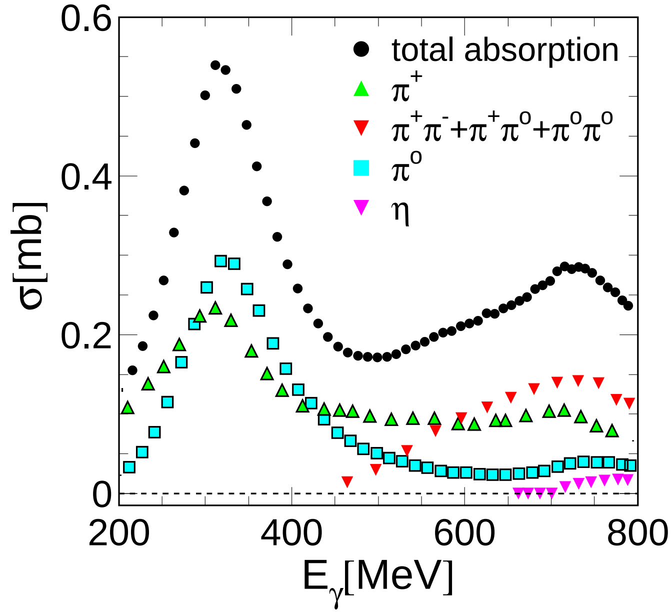

Figure 1.9: *Total photoabsorption on the proton and the different meson components. The importance of $\pi\pi$ channel in the second resonance region (mainly responsible of the bump shape) is clear.*

Due to its large contribution in the second resonance region (cf figure 1.9), the 2π channel is a logical choice to study this region . This channel is responsible of the bump structure in this region and carries half of the strength of the cross section.

Double pion production from the proton and the deuteron has been intensively studied in a series of experiments in particular by the DAPHNE (on the three $\gamma p \rightarrow N\pi\pi$ channels [24] and the $\gamma n \rightarrow p\pi^-\pi^o$ channel [25, 26]) and TAPS (neutral pion pairs photoproduction on proton [28, 29] and deuteron [27]) collaborations.

Many modes contribute to the double pion photoproduction. Some of them are shown in figure 1.10. In addition to the nucleon-Born terms, the nucleon can be temporary excited into a Δ resonance (Δ-Born terms) or in another N^* resonance, D_{13} or P_{11} (resonance terms). The two pions can be the products of a decay of another meson (ρ or σ-meson). Note that the ρ-meson never decays into two neutral pions and the σ-meson is an isospin zero particle that can only decay into neutrally charged pion combination.

The $D_{13}(1520)$ resonance (of which calculations in the Oset model [30] show the fundamental importance in the $\pi^o\pi^o$ channel as shown in fig. 1.11) could suffer from a large broadening from π and ρ mesons exchange [31, 32]. Then the resonance width gets sensitive to any modification of the π or ρ mesons spectral functions. Gomez Tejedor and Oset [30] pointed out that the peak structure of the

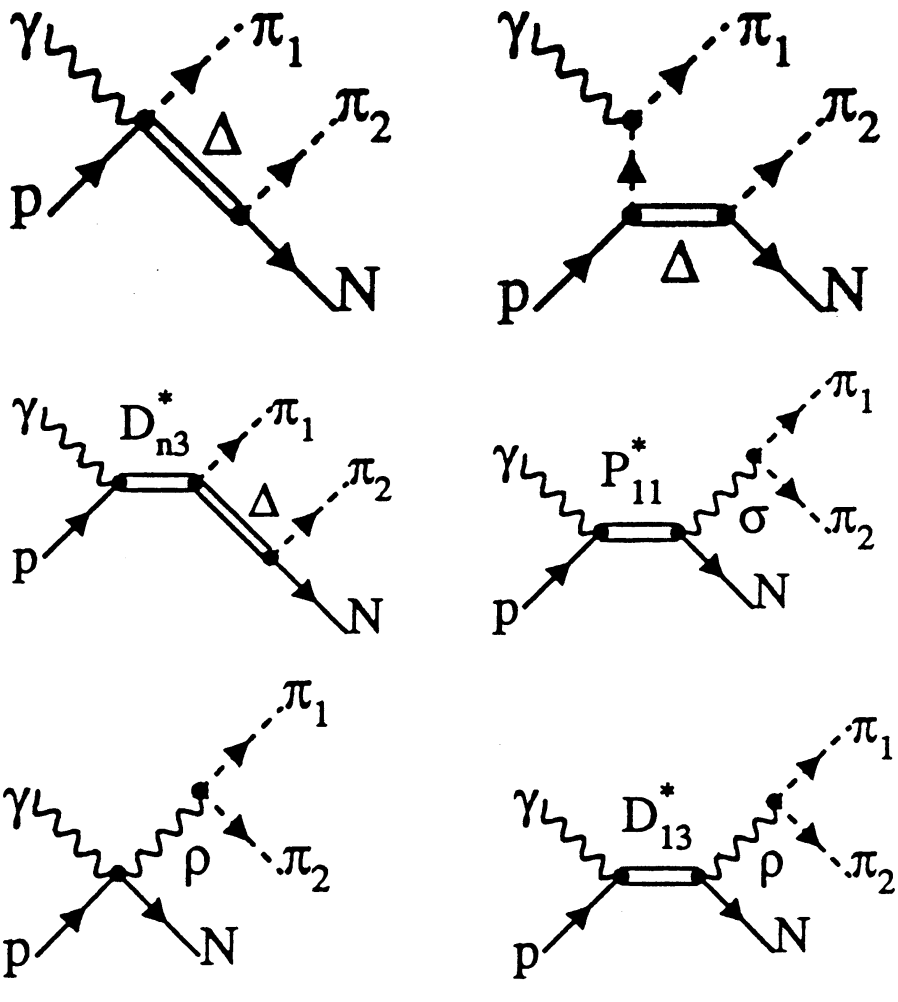

Figure 1.10: *Examples of* $\pi\pi$ *production modes.*

second resonance region is dominated by interferences of the Δ-Kroll-Ruderman term with the sequential decay of the D_{13} via the Δ resonance (only in the $\pi^+\pi^-$ channel). Hirata et al. [33] argued that this interference contribution (shown in the middle left diagram of fig. 1.10) is strongly changed in the nuclear medium and that would be one of the most important reasons for the suppression of the bump structure.

On the other hand, the ρ meson intermediate state is a large component for the $\pi^o\pi^\pm$ channel [32]. Models [30, 34] are unable to reproduce data in this channel if the ρ meson contribution is not taken into account (see fig. 1.12). This ρ contribution (that represents 20% of the D_{13} decay, see tab. 1.1) is only present in the $\pi^o\pi^\pm$ channel as the $\rho^o \longrightarrow \pi^o\pi^o$ is forbidden and contribution to $\pi^+\pi^-$ is suppressed as the ρ^o is not produced via the Kroll-Ruderman term. Any in

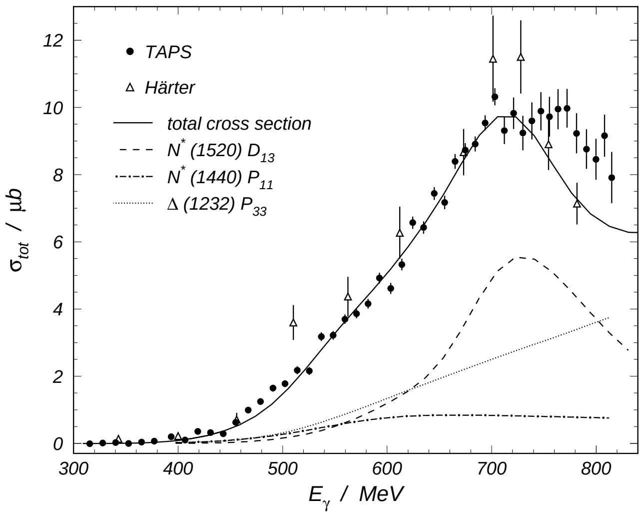

Figure 1.11: $\pi^o\pi^o$ *photoproduction from proton. Calculations by [39] show the importance of the* D_{13} *resonance in the second resonance region.*

medium particular behavior of the ρ meson would have a direct and fundamental influence on the $\pi^o\pi^\pm$ production.

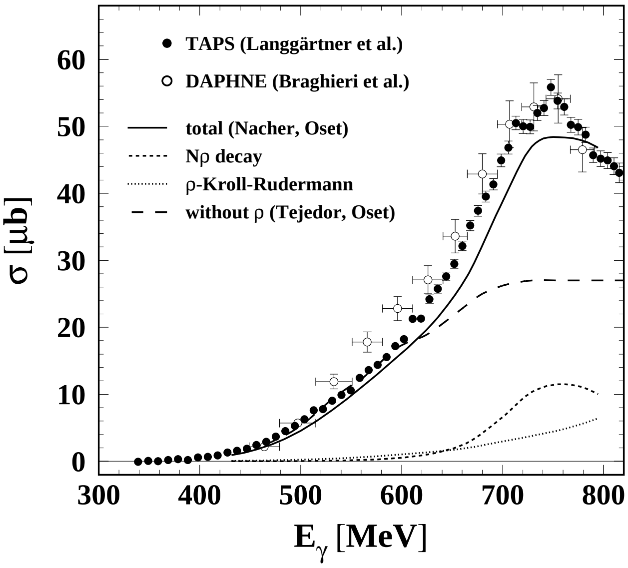

Figure 1.12: $\pi^o\pi^+$ *photoproduction from proton. Without the* ρ*-meson contribution (dashed curve), the model [39] can't reproduce the data.*

However, the in-medium behavior of the nucleon and its resonances in this region is highly non-trivial and very hotly debated. Data are needed to validate the models and try to understand better the subject. This work aims to produce double pion ($\pi^o\pi^o$ and $\pi^o\pi^\pm$) cross sections on calcium up to 820 MeV. Data have been taken on other targets (carbon and lead) during the same experiments in order to get precious comparison of the medium influence.

1.5 what kind of experiment is needed?

In order to study in medium effects, different targets are needed (carbon, calcium, lead) to scan over a large scale of average density. Pion induced reactions are limited by the initial state interactions. The pion mean free path (fig. 1.13) is shorter than 1 fm for usual pion induced reactions. In fig. 1.14, the density distribution of a calcium nucleus is shown to be smaller in the surface than in the center of the nucleus. In a pion induced reaction, the probe has a large probability to interact at the surface of the nucleus and almost never enters deeply. This makes the pion induced reactions only sensitive to a fraction of the density of the interior of the nucleus. This problem does not affect photoproduction reactions in which the photons can interact with the same probability at any depth inside the nuclei (fig. 1.15). It, indeed, can affect the pions produced in the nucleus that can interact before they can "escape" the nucleus. This is called final state interactions (FSI) and must be taken into account in the cross sections calculations.

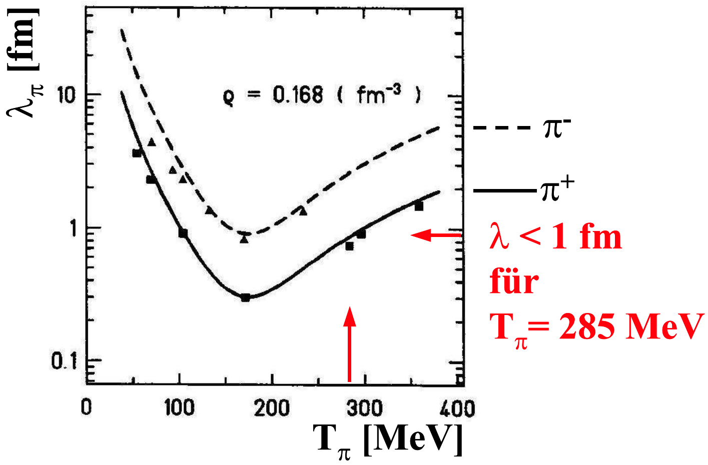

Figure 1.13: *Pions mean free path as a function of their kinetic energy.*

This work studies mainly the $\pi^o\pi^o$ photo-production events. Neutral pions are never directly detected as they decay within 10^{-16} s into two photons. In addition to a real photon source (MAMI accelerator with the Glasgow tagged photon spectrometer), good photon detectors are needed to perform this experiment.

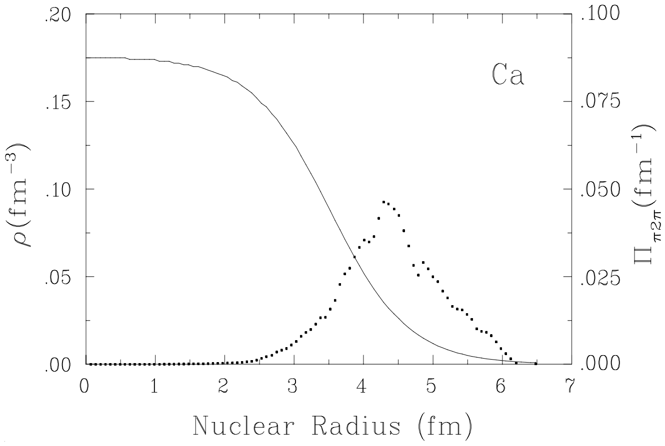

Figure 1.14: *Nuclear density distribution (ρ, solid curve) and probability of a $\pi 2\pi$ event to occur ($\Pi_{\pi 2\pi}$, dotted curve) for Ca as a function of the nuclear radius. The area subtended by $\Pi_{\pi 2\pi}$ is normalized to 1. (CHAOS collaboration)*

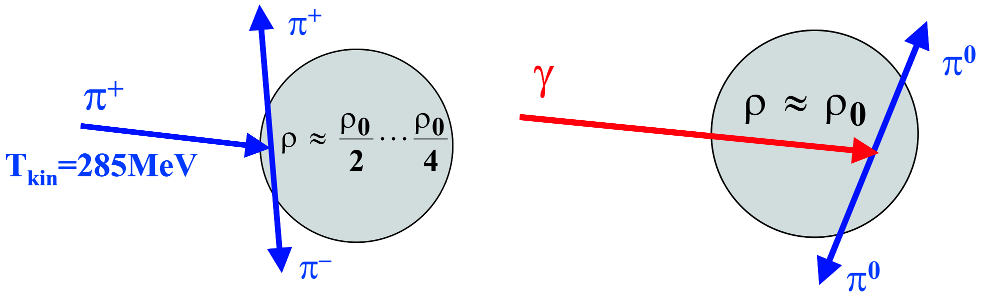

Figure 1.15: *pion beam only scan the surface so is sensitive to lower density than a photon beam scanning the full nucleus.*

Even not beeing the main task, these detectors need to be able to identify charged particles like $\pi^\pm$. This is the case with the TAPS spectrometer as detailed in the following sections.

Chapter 2

Setup

In order to perform a pion-photoproduction experiment, some tools are required.

- a tagged photon beam (produced by the MAMI [40, 41] accelerator and the Glasgow tagging spectrometer [42, 43])
- a target (calcium for this work)
- detectors efficient to detect the photons resulting from the neutral pion decays (TAPS [44] BaF_2 scintillators are used)
- a DAQ (data acquisition system) to record the detector signals

2.1 The photon beam

2.1.1 MAMI

The experiment was performed in the A2 hall of the Mainz Microtron (MAMI) facility [40, 41].

The photon beam is produced via bremsstrahlung from the MAMI electron beam. Electrons are accelerated in 4 successive linear stages based on cavity resonators that are supplied by 2.5 GHz klystrons.

Electrons of 100 keV are produced in an electron cannon and accelerated in the first stage up to 3.45 MeV in the injector linear accelerator (linac). Then, the electrons are injected in a succession of three racetrack microtrons (RTM). In each of the RTMs, the electrons fly several times through the linear accelerator. After each acceleration step, the electrons make a U-turn in a dipole magnet and fly back to another magnet to enter again the linear accelerator. As the two magnetic fields are constant the curvature radius increases at each step which requires different pipes for each return path until the maximum energy of the RTM is reached and the electrons are transfered to the next RTM.

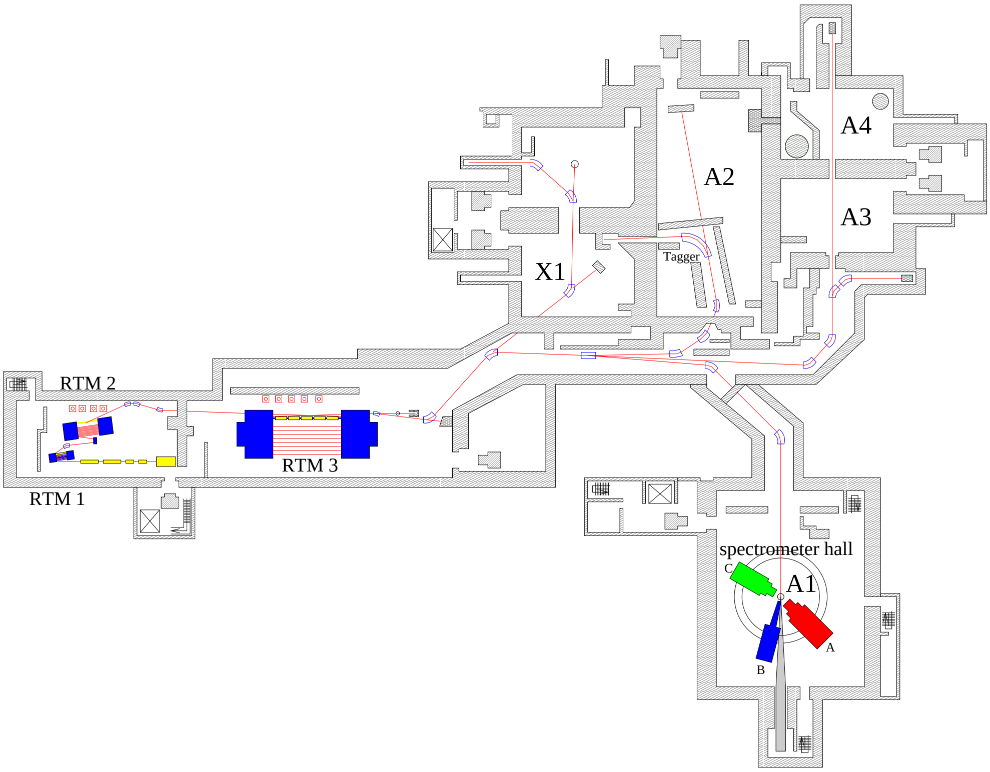

Figure 2.1: *General view of the MAMI accelerator, the experiment was set up in hall A2*

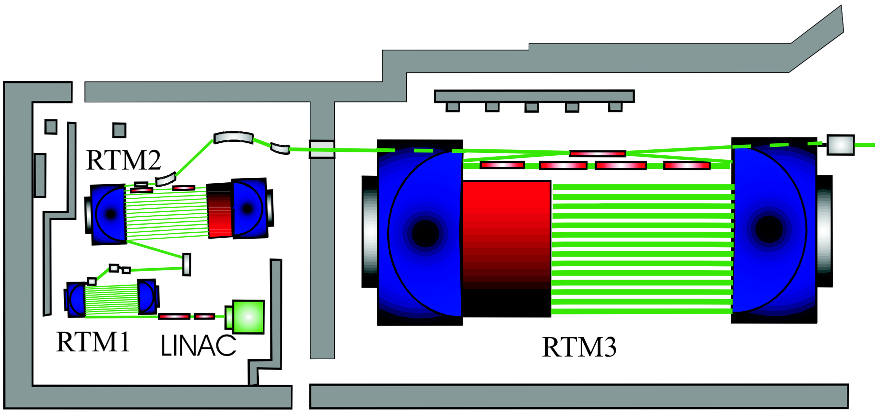

Figure 2.2: *MAMI accelerator with the linac injector followed by the 3 racetrack microtrons*

After the third RTM the electrons acquire an energy of 855 MeV with a maximum current of 100 μA. At lower beam intensities (tagged photon experiments can use only up to a few 100 nA), an operation mode with a maximum energy of 882 MeV is possible which was used for this experiment.

	linac	RTM1	RTM2	RTM3
maximum energy / MeV	3.45	14.35	179.7	855.0 (882.0)
number of cycles	-	18	51	90
dipole field / T	-	0.1026	0.555	1.284 (1.3260)
magnet weight / t	-	1.3	43	450

Table 2.1: MAMI features, for more details, see [40, 41]

2.1.2 The tagging spectrometer

The accelerated electrons are used to produce the photon beam. Electrons loose energy in a thin radiator (here a 4 μm thick nickel foil) via the emission of bremsstrahlung photons. The real photons that follow an energy (E_γ) distribution of $1/E_\gamma$ are used as a photon beam to excite nucleons of the target.

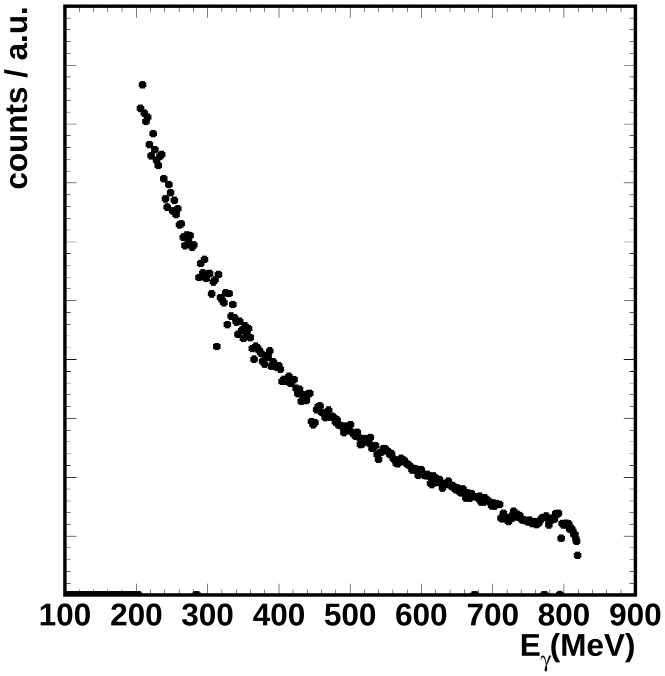

Figure 2.3: *Energy distribution of incident photons. Each point corresponds to a tagger channel. (data from this analysis)*

To study an event produced by an incident photon, the energy of this photon has to be known. The energy E_γ of a photon produced in the radiator is given by:

$$E_\gamma = E_0 - E_{e^-} \tag{2.1}$$

with E_0 the energy of the MAMI electron beam and E_{e^-} the energy of the electron after it produced the photon. This is valid as long as the energy transfered to the recoil nucleus in the bremsstrahlung process is negligible. This is true since, with a 99% probability, less than 2.5 KeV are transfered to the recoil nucleus.

For the determination of the incident photon energy E_γ, the scattered electron energy E_{e^-} has to be measured. This is done with the Glasgow tagging spectrometer (also called electron tagger) [42, 43].

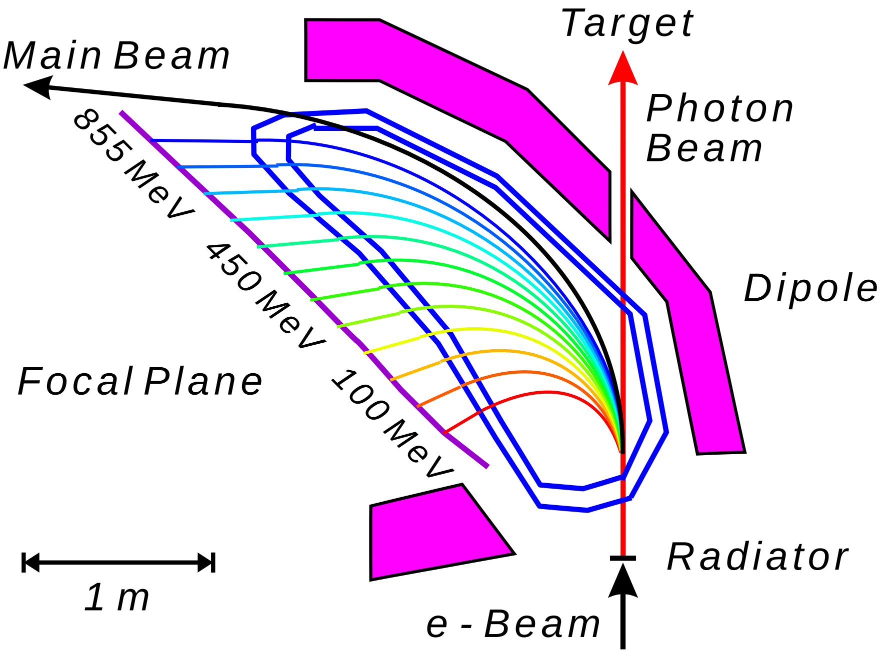

Figure 2.4: *The electron tagger, colored lines represent the electrons trajectory depending on their energy*

The electrons are horizontally deflected in a magnetic field (around 1 Tesla) produced by a dipole. The smaller their energy is, the more their trajectories are bended (see figure 2.4).

The electrons are detected in the focal plane of the spectrometer by 352 overlapping plastic scintillator of 2.4cm width which results in an energy resolution of 1 to 2 MeV for the electrons.

The bremsstrahlung photons are emitted in a narrow forward cone and an 8mm lead collimator is used between the radiator and the target to reduce the beam width (around 2cm on the target).

With this device, photons can be tagged in the energy range E_γ = 40-820 MeV. For the current experiment, a tagged photon range from 210 to 820 MeV was used.

2.2 The Ca target

The target was a 1cm thick disc of natural calcium (97% of ^{40}Ca). It had to be kept under vacuum since it oxidizes quickly in air. The parameters are listed in tab. 2.2 since the results of this work are compared to two other targets.
For the normalisation of the cross section, the number of Ca target nuclei per cm^2 is calculated as:

$$\mathrm{N}_{Ca} = \frac{\mathcal{N}_A \times \rho \times L}{M} = \frac{6.022.10^{23}(mol^{-1}) \times 1.54(g.cm^{-3}) \times 0.9907(cm)}{40.08(g.mol^{-1})} = 2.29 \times 10^{22}\ \mathrm{cm}^{-2}$$

Table 2.2: *Parameters of the nuclear targets.*

Target	**thickness** **[mm]**	**surface density** **[g/cm^2]**	**radiation length** **% of X_o**
^{12}C	24.989 ± 0.012	4.249 ± 0.008	10.1
^{40}Ca	**9.907 ± 0.007**	**1.54 ± 0.05**	**9.08**
^{nat}Pb	0.474 ± 0.006	0.54 ± 0.01	8.49

2.3 TAPS

TAPS [44] is an electromagnetic calorimeter built to detect photons, although it can also detect and identify particles as explained in the analysis section. It is made of 510 independent barium fluoride (BaF_2) scintillators. It has been used at several accelerators in different geometries. In this experiment, the detectors were arranged in 7 blocks surrounding the target. In front of each of these detectors, a thin plastic scintillator (called VETO) was placed to discriminate between charged and uncharged particles.

2.3.1 Principle

Except for the lower energy (below a few MeV) where Compton effect and photo-effect are competing, the main interaction mechanism of photons in the BaF_2 is e^+e^- pair production. The e^+ and e^- interact with the scintillator and produce bremsstrahlung photons which lead to other e^+e^- pairs. That produces a cascade of e^+e^- pairs and photons of decreasing energy which is called an electromagnetic shower. When the energy of the particles is low enough, their energy is populating the excited states of the scintillator. The light produced by the desexcitation of these states is called the scintillation light and is collected by the photomultipliers (PM) linked optically to the back of the scintillators. The electric signal produced by the PM is proportional to the amount of light and so proportional to the energy deposited by the particle.

2.3.2 BaF$_2$

A very interesting feature of the barium fluoride scintillators (with their good energy and time (Δt < 200 ps) resolution) is their two different scintillation components. A fast one with a decay time of τ=0.6 ns and a slow one with a life time of τ=620 ns. The ratio of these two components depends on the ionization density and therefore differs for different particle species. Photons for example have more light in the fast component compared to the slow component than heavier particles like protons or α particles. Measuring the collected light in two different time windows (40ns and 2μs) and comparing their ratio helps to identify the particle type.

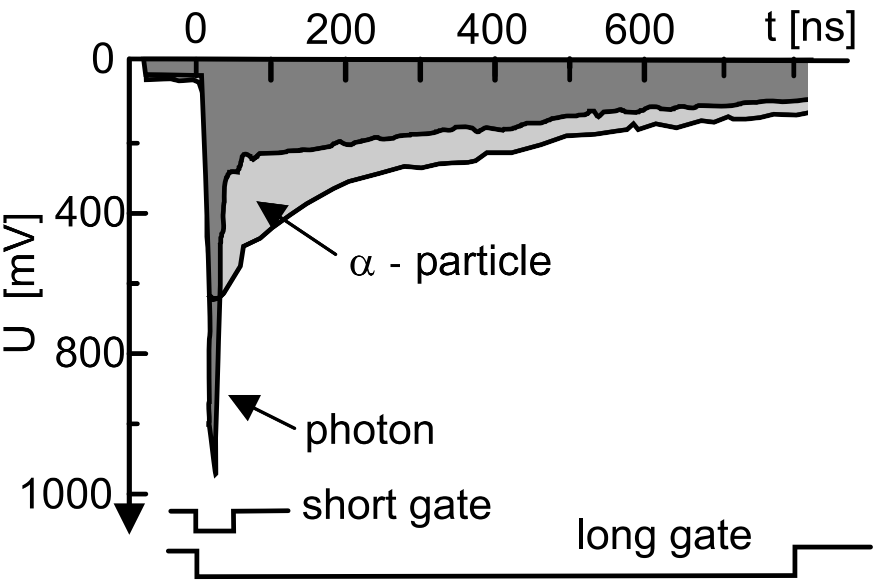

Figure 2.5: *typical pulseshape representation for an alpha particle and a photon signal in the BaF$_2$*

2.3.3 Single Detectors

Each single barium fluoride crystal has a hexagonal section. They are 25 cm long and have an inner diameter of 5.9 cm.

This geometry has been chosen as a good compromise between a small size allowing a good spatial resolution and a large enough size to collect enough energy in each detector and to keep the shower in a limited amount of detectors in order to achieve a reasonable energy resolution. Each crystal is coupled with optical

Figure 2.6: *picture of a single* BaF_2*crystal and a fully mounted detector element with its photomultiplier where the crystal is covered with black tape*

density		4.89 g/cm^3
radiation length		2.05 cm
moliere radius		3.4 cm
fast component	wavelength lifetime	195 nm, 220 nm 0.6 ns
slow component	wavelength lifetime	320 nm 620 ns

Table 2.3: BaF_2properties

oil to a photomultiplier tube.

2.3.4 Veto Detectors

In front of each BaF_2 crystal, a 0.5 cm thick plastic scintillator is mounted. These veto detectors are read out by photomultipliers through light guides. They discriminate between charged and uncharged particles as these detectors are fired only by charged particles and are insensitive to neutral particles like photons.

2.3.5 Geometry

510 BaF_2were used in this experiment. They were arranged in 6 equivalent blocks plus a larger wall placed in the forward direction (FW wall). The 6 smaller walls are arrays of 8×8 elements and the larger forward wall had a rectangular shape made out of 138 elements. The walls surrounded the target as shown in figure

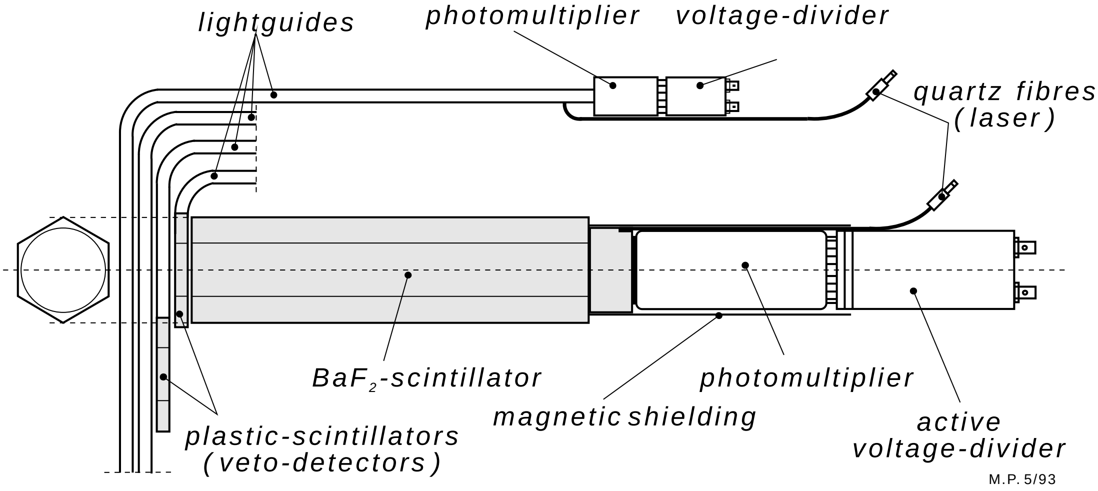

Figure 2.7: *drawing of a BaF_2scintillator with its photomultiplier and veto detector*

2.8. The distance to the targets and the polar angles with respect to the beam line are given in table 2.4. The setup covered approximately 40% of the full solid angle.

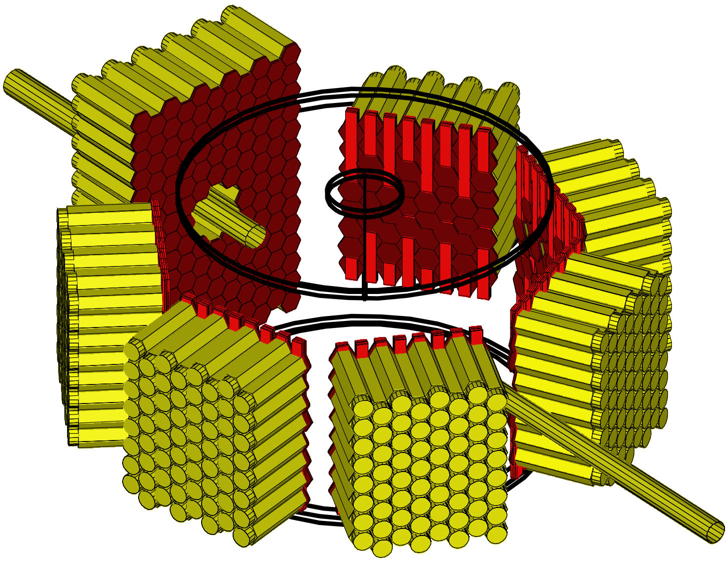

Figure 2.8: *geometry of the setup, the target vacuum chamber limits are drawn between the BaF_2walls. The photons fly in the beam line from right to left. The distance from the detectors to the target is around 55 to 60 cm (see table 2.4).*

The primary photon beam passes through a hole in the center of the forward wall and is stopped in a beam dump.

block name	polar angle	distance to target
A	152.6°	57.3 cm
B	103.6°	58.5 cm
C	54.6°	57.3 cm
D	-54.4°	55.9 cm
E	-103.4°	56.3 cm
F	-152.4°	55.9 cm
FW	0.0°	55.0 cm

Table 2.4: Positions of the 6 smaller blocks (A-F) and the large forward wall (FW)

Figure 2.9: *picture of the setup, the target is here an helium target and the beam comes from the upper left side*

2.4 electronics

When an event is produced in the target, different particles (photons, mesons, nucleons, ...) are emitted and detected in the BaF_2 detectors.

When a particle interacts with a crystal, scintillation light is produced. A photomultiplier (PM) converts the scintillation light into an electric pulse of 0.1 - 1 Volt. The total charge in the electric pulse is proportional to the energy of the incident particle, although the proportionality constant depends on the type of the particle. This signal, together with the signals from every other BaF_2 has to be read out and analyzed to decide whether or not it is relevant to record the event on tape.

The signal from each BaF_2 is first splitted into four equal signals.

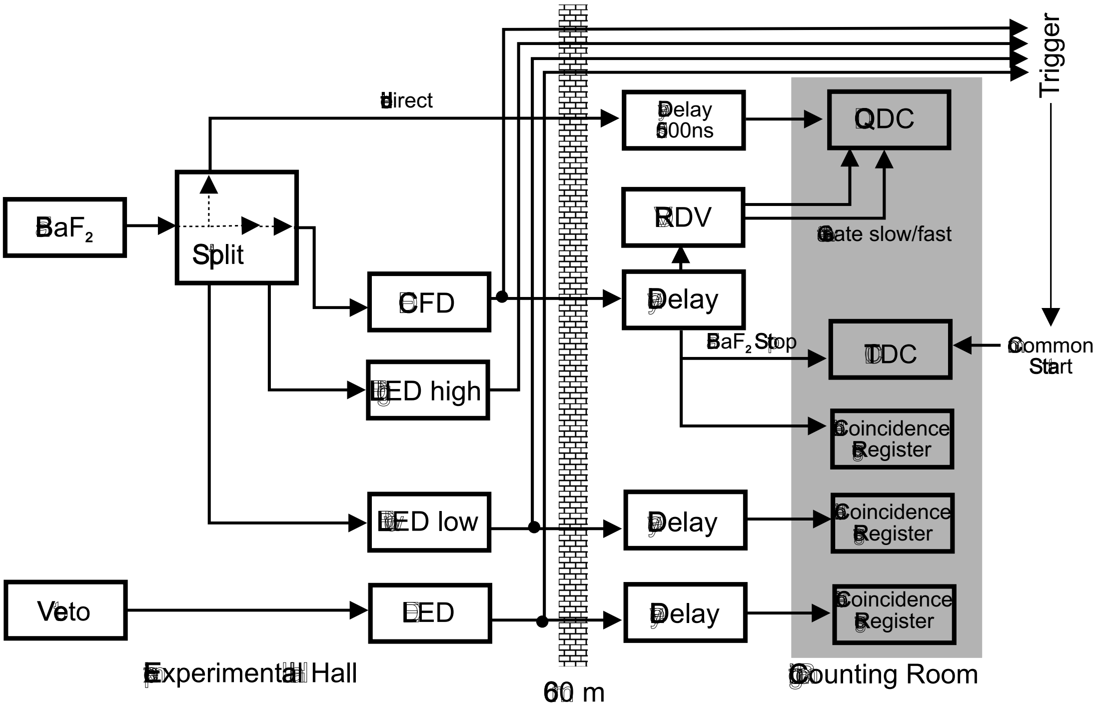

Figure 2.10: *Schematic drawing of TAPS readout electronics for a single detector element. The information given by electronic modules in the gray area is recorded on tapes.*

Two of them are sent to LED (Leading Edge Discriminator) modules that check if the signal exceed a given threshold. One of the signals is compared to a low threshold (called LED low) of 10-20 MeV and the other to a higher threshold (called LED high) of 50-60 MeV. From these informations (what detector signal exceeded the LED high and LED low threshold), logical operations are made to decide if the event is interesting for the experiment and if it is useful to record it. The trigger required that a certain amount of different TAPS blocks were fired (for this purpose, the large forward wall was logically cut into 4 parts). A fired block is a block where at least one detector saw a signal larger than the LED (low or high) threshold. Different trigger conditions can be used at the same time. But, as some conditions are much easier than other to fullfil, the dead time of recording of these common events would make very small the recording rate of more restrictive trigger conditions. In order to compensate that, a downscaling

LED	**multiplicity**	**downscaling factor**	**fraction of recorded events**
low	1	2999	1 / 3000
low	2	49	1 / 50
low	3	0	1 / 1
high	2	0	1 / 1

Table 2.5: downscaling factor with the compared LED (high or low), the multiplicity (number of fired block required), the downscaling factor and the fraction of recorded events (equal to the downscaling factor plus 1)

factor is applied to these easy conditions, in other words, only 1 out of a certain amount of events of the kind is recorded. The downscaling factors are summarized in table 2.4.

For the $\pi\pi$ analysis, the trigger condition required is LED low with a multiplicity of 3: in three different blocks (or more), at least one detector produced a signal larger than the LED low. The LED high 2 condition was used for the measurement of the production cross section of eta mesons in the $\eta \rightarrow \gamma\gamma$ channel The third signal (from the split module) is compared to another kind of threshold module called CFD (constant fraction discriminator). The output of this module is independent of the signal height and is used for the timing information of the signal. The detectors for which the signal exceeds the CFD threshold will be recorded if the event is accepted by the trigger conditions on the LED thresholds. The output signal of the CFD modules is used 3 times.

- To produce the bit pattern of what detectors fired (signal larger than the CFD threshold) using a coincidence register.
- As input for the TDC (time to digital converter) modules which determines the time difference between this event and a common time reference for the 510 BaF_2 signals.
- As input for an RDV module (retard à durée variable) which generates the integration gates for the QDC's (charge to digital converter). The QDC's integrate the 4^{th} signal (from the split module) to determine the energy of the detected particles. The QDC's integrate the signal over two gates, a short one of 40 ns to cover the fast component of the BaF_2 and a long one of 2μs to integrate over the full signal (including the slow component).

Each VETO detector signal is compared individually to a LED threshold and a bit pattern of the fired vetos is produced (what VETO produced a signal larger than its LED threshold).

In summary, the signal of each BaF_2 scintillators is compared to LED thresholds and the combination of each of these patterns (what detector signals are larger than the thresholds) decides if the event is recorded. If the event is accepted, its energy and timing information are recorded for those BaF_2 detectors, for which the signal exceed the CFD threshold.

The events are recorded on DLT tapes and the next chapter will explain how in a later offline analysis, the recorded informations can be analyzed to identified the detected particles of those events.

More details on the electronics can be found in [45].

Chapter 3

Data Analysis

This chapter will explain, how in an offline analysis, photons and particles are identified and how their energies and directions with respect to the target and beam are reconstructed. The final result of this analysis are particle types and four-vectors for each detected hit in all events. A selection of the investigated reaction is then possible (for this work, 2 pions were produced via the γ N $\rightarrow \pi\pi$ N were selected).
What are the available informations in the raw data?

- The first information is which detectors have fired during the coincidence time . This information is stored as a bit pattern which is simply a list of 0 and 1. 1 if the corresponding detector has been hit, 0 else wise. 3 different bit patterns were produce for each event. One concerning the CFD information (with a threshold of 1 to 2 MeV), the LED low information (threshold of 10 to 20 MeV) and the veto detectors information is the third one.

- Then for each of the hit BaF_2 detectors, informations related to the energy and time have been stored. This informations are the channel numbers of the QDC (energy) and TDC (time) of this detector. These numbers are not physical quantities but will be converted in meaningful values (energy in MeV and time in ns) with some calibrations which will be detailed in the following.

- The tagger produces an extra bit pattern from the tagger that tells us which of its detectors received an electron at a time close to the event (it was discussed before that many electrons hit the tagger in short time due to the high flux of incident electrons given by the MAMI accelerator). The time information of each fired scintillator is also recorded.

- One also needs to know how many incident photons hit the target in order to convert the number of detected events into cross sections (probability for an incident photon to produce in the target an event of the studied type). Tagger scalers count the number of scattered electrons, which, once corrected with the tagging efficiency, corresponds to the number of photons passing the target. The tagging efficiency depends mainly on the collimator size (8mm in this experiment).

The three analysis step are required for each event. First, the raw information have to calibrated into physical quantities. Then these quantities are used to identify the primary particles (particles that hit the detectors, like photons or protons). Finally, neutral mesons produced in the target are reconstructed out of detected pairs of primary photons (typically $\pi^o \rightarrow \gamma\gamma$).

3.1 calibrations

3.1.1 energy calibration

The energy information for each BaF_2 is the integer output of the QDC modules. This not-yet physical quantity has to be converted into an energy. The calibration is made individually for each BaF_2 scintillator and for both the short and the long gate (the long gate is used as the particle energy and the comparison with the short gate is used to identify its type as explained in the pulseshape section). In order to do this calibration, special runs to measure cosmic muons have been made in the beginning of the experiment. Another run is made in the end to check the stability of this measurement. The beam is switched off and the cosmic radiation is measured. A typical spectrum shows two interesting points (see figure 3.1). The “first non-zero value” is called the pedestal, and corresponds to a value of the energy of zero. The second point is the peak value. It results from the minimum ionizing particles (in particular muons). Simulations have shown that due to the scintillator shape and position, this peak corresponds to an energy of 38 MeV.

The two points are enough for the calibration thanks to the linearity between the measured channel number and the deposited energy [46].

This calibration aims at a relative calibration between the detectors. A second order calibration using the mass of neutral mesons will be applied later.

3.1.2 time calibration

The raw timing signal is measured with respect to a reference signal and has to be converted into a useful time-of-flight of the detected particles.

Such a time-of-flight is the difference between the time arrival of the incident photon in the target and the time of the detection of the produced particles in the BaF_2. The arrival time of the incident photon on the target follows from the

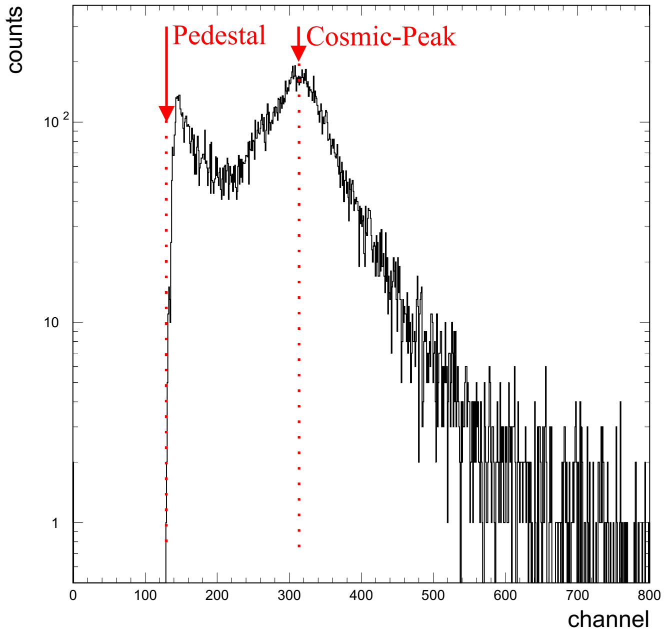

Figure 3.1: *Spectra of cosmic rays in QDC channels of a single BaF_2 detector. The two points shown (pedestal $E = 0$ MeV and peak $E = 38$ MeV) are used to calibrate this detector.*

time information of the scattered electron which is detected in the focal plane of the tagging spectrometer.

TAPS time calibration

The absolute time calibration is derived from dedicated measurements. For this measurements, a signal is split into two parts, one is led directly to the start of the TDC's while the other passes through a cable delay of known lengths before it is led to the stop of the TDC's. The delay of the cables are measured with an oscilloscope. Using several cables of different length (ie different delays from 3 ns to 50 ns), an individual channel to time calibration is obtained for each TDC module.

tagger time calibration

Each tagger TDC gets the same treatment as the TAPS TDC. The delay cables are here replaced by a time calibration module which produces sharp pulses every 10 ns (ORTEC Time Calibrator module Model 462).

TAPS-tagger time calibration

Up to now, the time information for TAPS and the tagger has been calibrated in ns. But this is still a timing with respect to an arbitrary common time reference

signal. The respective timing for the tagger and TAPS detector modules with respect to this reference signal ("pre-trigger") is given by:
t_{tagger} = pre-trigger - indiv tagger scintillator
t_{TAPS} = indiv TAPS detector - pre-trigger

Simply adding these two times gets rid of the meaningless pre-trigger time (the common reference) :
$\mathrm{t}_{TAPS-tagger} = \mathrm{t}_{TAPS} + \mathrm{t}_{tagger}$
$\mathrm{t}_{TAPS-tagger}$ = indiv TAPS detector - indiv tagger scintillator

This value is exactly what is needed. It is related to the time-of-flight of the detected particles. The off-set is calibrated so that the time is zero when the detected particle was a photon (the time gets larger if the detected particle is slower).

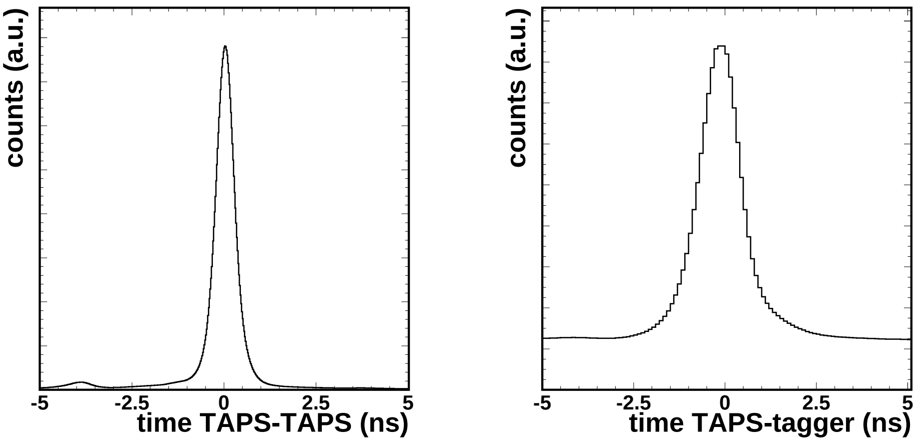

Figure 3.2: *Effect of time calibrations. Left: relative time of two photons detected in TAPS. The small peak around t = -4 ns is due to events where an incident photon hits directly a* BaF_2 *near the beam line before reaching the target (see figure 2.8) and the electromagnetic shower produce another photon escaping the* BaF_2 *which goes mainly forward and hits the forward wall. The time difference is the time of flight of the second photon which is around 2 times the time-of-flight for a photon to travel the distance target-detectors (2×55cm):* $\Delta t = 2\times 0.55(m) / 0.3(m/ns) = 3.7$ *ns). Right: relative time of a photon detected in TAPS and an electron detected in the tagger.*

In principle, one should calibrate the signal for each combination of a single TAPS detector vs a single tagger scintillator but there are too many combinations (510 TAPS det × 352 tagger scintil = 179520 combinations). A more efficient way is an iterative procedure. In the first step, the timing spectra for all individual TAPS detector are compared to the "OR" of all tagger channels and shifted to zero for photons events. In the next step, all individual tagger channels are compared to the "OR" of the TAPS detectors and then the procedure is iterated. After some iterations, a time resolution TAPS-tagger around 1.2 ns and a time resolution TAPS-TAPS (time difference between two photons, coming from the decay of a π^o for example) around 0.55 ns is achieved.

3.2 identification of primary particles

After the above procedure, the time-of-flight (in ns) and the deposited energy (in MeV) is known for each TAPS detector. One must now convert that into "particles". The first step is to arrange into clusters the detectors fired by the same particle. The second step will be to identify the particle (is it charged? is it a photon?).

3.2.1 cluster identification

When a particle interacts with the BaF_2 of a detector, it creates an electromagnetic shower which is a succession of e^+/e^- pairs and bremsstrahlung photons emission. This shower is quite large and spreads over several neighbor detectors. One must find out which detectors are part of the same shower and add their energy to have the full particle energy. The bunch of detectors fired by the same particle is called a cluster. The identification of a cluster starts with any fired detector to which is added any fired neighbor. The relative time between neighbors must be smaller than 4 ns to be sure that the 2 detectors have been fired by the same shower. Detectors are added to the cluster as long as new fired neighbors of a member of the cluster can be found (within the 4 ns). Once a cluster has been fully determined, the detector with the largest energy deposited is called "central detector" of this cluster.

3.2.2 VETO

The VETO detectors are, as explained in section 2.3.4, used to discriminate charged and neutrals particles. As the efficiency of the VETO detectors is limited, the VETO information is never used to identify charged particles, but is used to reject charged particles when seeking for neutral particles (like photons).

3.2.3 pulseshape

As explained in section 2.3.2, a particularity of BaF_2 is to have scintillation light with two different frequencies and decay times and that the ratio of these two components is different for photons and other particles. This feature can be used to identify particles. Integrating the output signal of the BaF$_2$ over a short gate (40 ns) gives an information on the fast component (E$_{short}$). Integrating it over a long gate (2 μs) gives an information of the total (fast + slow) light output (E$_{wide}$). The ratio of these two measured energies E$_{short}$ / E$_{wide}$ is in the order of 1 for photons (due to the energy calibration) and is smaller than 1 for particles (as the fast component is less important than for photons).

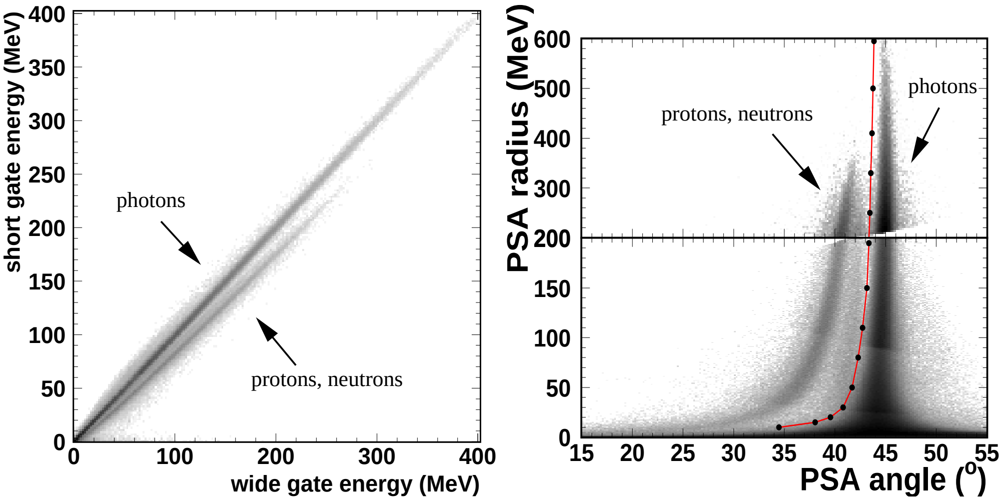

Figure 3.3: *Typical pulseshape plot for a BaF$_2$ detector of the forward wall. Left: E$_{wide}$ (full energy) is plotted vs E$_{short}$ (only the fast component). The photons lie on a line E$_{wide}$=E$_{short}$. Right: same plot using polar coordinate (explained in text). Photons are chosen as being to the right of the line. Both representations use a logarithmic scale as most detected particles are photons.*

As can be seen in the figure 3.3 left, a selection E$_{wide}$ vs E$_{short}$ is not easy. Plotting the same points in polar coordinates makes the selection much more efficient (figure 3.3 right). One axis is the radius of the point ($R = \sqrt{E_s^2 + E_w^2}$) and the other is the angle ($\phi = arctan(E_s/E_w)$) where E$_s$ is the short gate energy and E$_w$ the wide gate energy. In such a plot, the photons are in principle aligned on a vertical line for $\phi = 45$ degrees, and the particles on a line at smaller angle. Each BaF$_2$ can be calibrated by the determination of a curve between these two set of points and one can identify photons as particles lying at larger angle for a given radius, and particles as lying at smaller angler than the curve.

Pulseshape is not adapted for $\pi^{\pm}$ selection. Charged pions PSA is due to the muon decay not very well defined and they lie in a PSA plot between photons and protons which makes it very difficult to select them this way. Pulseshape was for this work only used to identify photons.

3.2.4 impact position

A cluster (set of detectors fired by the same particle) has been identified. The kind of particle that produced it (photon or charged particle like charged pion or proton) is known and also its deposited energy and time-of-flight. A precise impact position is still required (better than "somewhere in the cluster"). With such an information the four-vector of the particle would be fully determined (at least for photons as for charged particles one also needs its mass).

photons

It's a general feature of detectors that when the signal is spread on several elements, the spatial resolution is better than the size of on element thanks to basic barycentre methods. This also the case here. The impact position has to be corrected as the shower develops inside the BaF_2 and the particles enter with a certain angle in respect to the normal (this angle is indeed larger at the edge of the blocks than in the center). The signal position has to be extrapolated to an impact position between the particle and the BaF_2. A position resolution of 2 cm can be achieved for a 300 MeV photon [46] which means an angular resolution of 2 degrees.

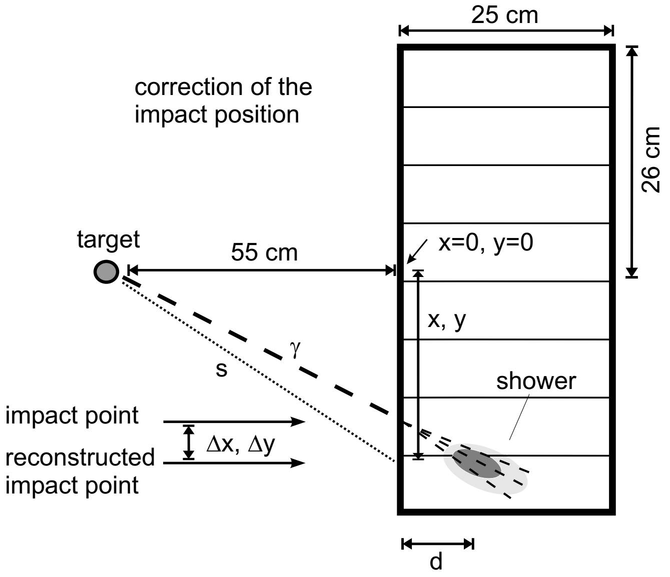

Figure 3.4: *Correction of impact position of photons.*

To determine the shower position, the barycentre method (average the position of the center of each detector of the cluster weighting them with the deposited energy in this detector) has to be defined as the low energy detectors are taken too strongly into account. The weight is replaced by a more realistic weighting factor for each element i of the cluster [47, 48] :

$$W_i = \max\{0; 5 + \log \frac{E_i}{\Sigma E_i}\} \tag{3.1}$$

Together with the position of the shower, its depth in the BaF_2 crystal has also to be known. It can be calculated as [49]:

$$d = X_0.(\ln \frac{E}{E_c} + 1.2) \tag{3.2}$$

E is the shower energy in MeV and $E_c = 12.7$ MeV is called the critical energy. $X_0 = 2.05$ cm is the radiation length of the BaF_2. The corrections ΔX and ΔY which have to be applied to the cluster position is given by:

$$\frac{\Delta X}{X} = \frac{\Delta Y}{Y} = (\frac{s}{d} + 1)^{-1} \tag{3.3}$$

where d is the depth of the shower and s the distance from the target to the center of the shower.

particles

The case of charged particles is quite different due to the narrow shower they produce. The cluster usually consist of a single detector. To avoid an angular distribution made of peaks at the center of each detector, once a detector is recognized as a charged cluster, the position (x and y coordinates) is randomly chosen on the surface of this detector. This is not the exact position but at least leads to smooth physical angular distributions with a resolution of the size of a detector.

3.3 identification of neutral mesons

Four-vectors of detected photons have now been determined. Neutral mesons (π and η) have a very short life time, so only the photons resulting from their decay are detected ($\pi^o \rightarrow \gamma\gamma$ at 98.8% or $\eta \rightarrow \gamma\gamma$ at 39.4%). The four-vector of a neutral meson is equal to the sum of the four-vectors of the two photons resulting from its decay. Each of these two photons have an invariant mass (square of the four-vector) of zero but the photon pair has a non-zero mass (the mass of the neutral meson). This way, adding up four-vectors of photon pairs, neutral mesons can be identified via their mass and reconstructed.

3.3.1 invariant mass analysis

When a particle decays, its four-vector is conserved. In the case of a π^o or an η that decays into 2 photons, the sum of the four-vector of the two photons is equal to the four-vector of the original meson (π^o or η). Then the mass of this reconstructed meson is the square of the four-vector (E^2 - $\vec{p}^2$). If the mass is the mass of a π^o or the mass of an η (within a certain width), these two photons can be identified as a meson of this type. With the two photon four-vectors called P_1 and P_2, the invariant mass of the meson (of four-vector P) can be written :

$$M_{inv} = \sqrt{P^2} = \sqrt{(P_1 + P_2)^2} = \sqrt{P_1^2 + P_2^2 + 2P_1P_2} \tag{3.4}$$

As P_1 and P_2 are the four-vectors of photons, $P_1^2 = P_2^2 = M_\gamma^2 = 0$. The invariant mass of the photon pair can be written:

$$M_{inv} = \sqrt{2P_1P_2} = \sqrt{2E_1E_2.(1 - cos\phi_{12})} \tag{3.5}$$

With E $_1$ and E_2 being the energy of the two photons and ϕ_{12} the opening angle between them.

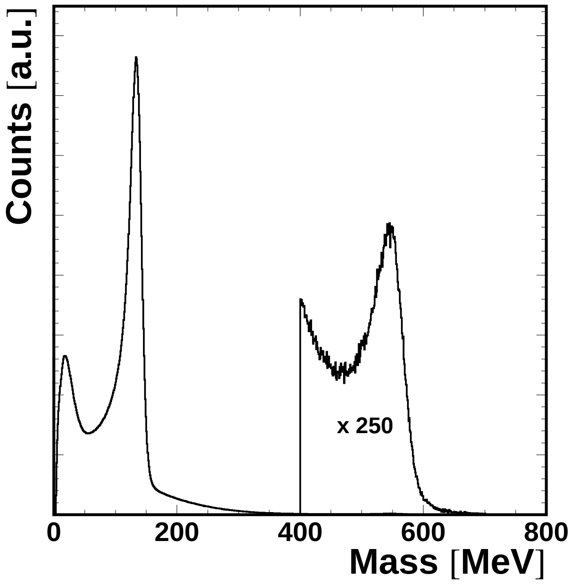

Figure 3.5: *Invariant mass of photon pairs. The peak at 135 MeV is made of photon pairs coming from a π^o desintegration. The second peak at 547.3 MeV is made of photon pairs coming from an η meson desintegration (× 250). Some background can be seen (strong at low mass) coming from combinations of uncorrelated photons.*

A spectrum of the invariant mass of any combination of two photons (figure 3.5) shows two peaks (one for the π^o and the other for the η) plus a so called combinatorial background coming from combinations of photons that do not come from the same meson (and for which the mass can be anything and is meaningless).

3.3.2 energy correction

When looking at the pion pair masses, the π^o and the η peak can be identified but they do not correspond exactly to the correct mass. A second step of calibration has to be done after the energy calibration with cosmics which was mainly a relative calibration of all detectors.
To do so, a second degree correction has to be applied to the energy of each photon in order to make both π^o and η peak fit to the correct mass value (resp. 134.9766 MeV and 547.30 MeV).

$$E'_\gamma = a \times E_\gamma + b \times E_\gamma^2 \tag{3.6}$$

The parameters a and b are chosen so that the reconstructed meson masses are correct. The best parameters are found to be a = 1.2 and b = -2.7 × 10^{-4} MeV^{-1} for that data. The result of this calibration can be seen in figure 3.5.

3.3.3 summary of neutral mesons selection

A neutral meson is identified in an event when the following conditions are fullfiled.

- two photons are found and their energies are corrected
- coincidence within a small time window is required for the two photons
- the mass of the pair of photons is calculated and compared to the π^o and η mass
- the four-vector of the neutral meson is calculated as the sum of the four-vectors of the two detected photons so that the meson is fully determined

3.4 identification of charged particles

All kinematic variables of photons and neutral mesons are now determined. What about the charged particles? Their impact position is determined and so assuming that they come from the target, their direction of flight is also determined. The energy deposited by a detected particle is known and can be assimilated to its kinetic energy. Only the mass of the particle is missing (is it a proton, a pion, an electron, ...) to determine it completely. Many experiments use a magnetic field. This way, measuring the trajectory of the particles (curvature) and their kinetic energy, it is trivial to identify them (and also to know if the particle is positively or negatively charged, depending on which side it is bended). The setup of this experiment has no such magnetic field so other methods are required.

3.4.1 TOF/energy

The time-of-flight of the particles has been calibrated. As the geometry of the detectors and the impact position are known, the distance of flight is also known. For a particle of a given mass and a given kinetic energy, the time-of-flight is indeed constant. If the time-of-flight is normalized to a 1 meter flight and plotted versus the kinetic energy (deposited energy is here the related available information), particles of the same mass would be theoretically aligned on one curve. This way one can select charged particles of a certain kind (electrons, charged pions, protons and even deuterons) (see figure 3.6).

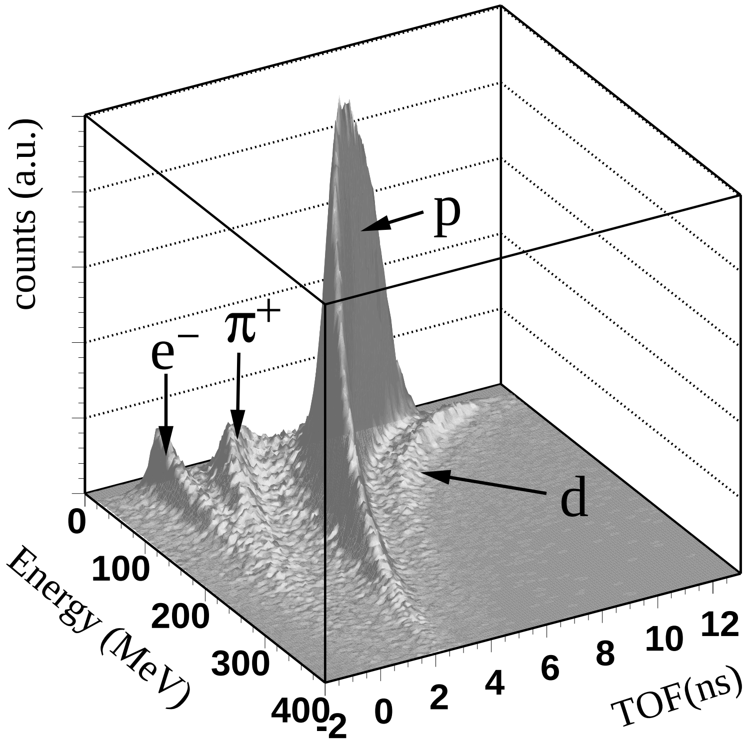

Figure 3.6: *Time-of-flight versus energy plot for charged particles for incident photon energies of 400 to 460 MeV (after a first* π^o *has been identified). We can select deuterons (d), protons (p), charged pions (*π^+*) and electrons (*e^+*). Note that many protons can be found and the large proton bump contaminates partly the pion band; this selection is not 100% efficient. Due to the time calibration, a particle flying with the speed of light (photon) would have a time-of-flight of zero.*

3.4.2 pion tof correction

As the time-of-flight is more precisely known than the kinetic energy, if the type of the particle is known, the kinetic energy can be calculated with a better precision using the time-of-flight information and the mass of the particle.

The efficiency of this kinetic energy correction can be checked with the background-free channel: $\eta \rightarrow \pi^o \pi^+ \pi^-$ (28.0%). If one neutral pion and two charged pion are identified together, they should result from a η meson decay. The square of the sum of the four-vectors of the three pions should then be equal to the mass squared of an η.

$$(P_{\pi^o} + P_{\pi^+} + P_{\pi^-})^2 = P_\eta^2 = M_\eta^2 \qquad (3.7)$$

with P_{π^o}, P_{π^+}, P_{π^-} and P_η being respectively the four-vectors of the π^o, π^+, π^- and of the reconstructed η.

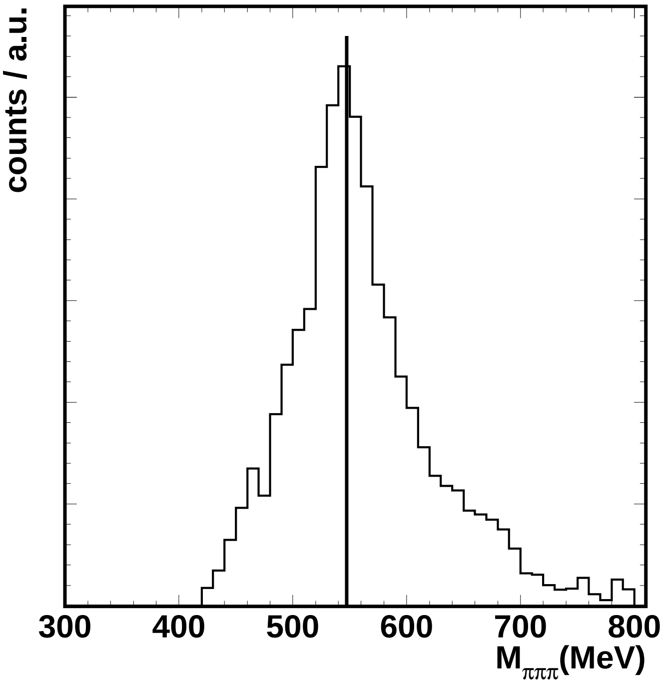

Figure 3.7: *Mass of* $\pi^o\pi^+\pi^-$ *used to calibrate charged pions time-of-flight after this calibration is applied on the charged pions. The line is at* M_η *= 547.3 MeV.*

A peak can be identified in this distribution but it does not correspond exactly to the η mass. It turns out that a constant offset has to be added to the time-of-flight of pions to get the correct kinetic energy. For this work an optimal offset of Δ_t = -0.3 ns has been empirically found to correct the time-of-flight of charged pions in order to calculate their kinetic energy. With this offset, the mass of $\pi^o\pi^+\pi^-$ is at the correct position ($M_{\pi\pi\pi} = M_\eta$ = 547.3 MeV) as shown in figure 3.7.

3.4.3 summary of charged pion selection

- particles are selected in the pion band in a time-of-flight vs energy plot
- the offset to the time-of-flight is applied (Δ_t = -0.3 ns)
- the kinetic energy is calculated with the corrected time-of-flight and the mass of the charged pions (139.57 MeV)
- the four-vector of the pion is calculated with its kinetic energy, the pion mass and its direction of flight so the charged pion is fully determined

3.5 identification of $\pi\pi$ events

More complex events than single particles can be also identified with chosen criteria. Here also, one must always make a compromise between elimination of background (not miss-identifying other types of events) and rejecting as few good events as possible.

3.5.1 missing mass principle

Two different types of background can be found. Miss-identification of a particle (a proton recognized as a pion for example) or some particles belonging to the event have not been detected due to the limited solid angle (the typical case for this work is when an η is produced, it decays into $3\pi^o$, two of them are detected and identified as a two pion events which it is not). Most of background of the last type can be avoided using a missing mass analysis.

In other words, the principle is to calculate the mass of what is missing (ie, what is not detected). In the case of a $2\pi^o$ event (γ N $\rightarrow$ $\pi^o\pi^o$N), 4 photons are identified out of which $2\pi^o$ are reconstructed. All informations about the initial state are available: the energy of the incident photon and its direction (along the beam axis), and the target nucleon is assumed at rest. Everything is also known about the two pions (their four-vectors). So the reaction is there γ N $\rightarrow$ $\pi^o\pi^o$X where X is not detected. A “good” event would have a nucleon as X. Then as the four-vectors are conserved, the four-vector of X is:

$$P_X = P_\gamma + P_N - P_{\pi_1^o} - P_{\pi_2^o} \tag{3.8}$$

The mass of X can be calculated as the square of its four-vector. If M$_X$ is the mass of a nucleon, this is a “good” event (γ N $\rightarrow$ $\pi^o\pi^o$N). If not, this is a “bad” event (like the event : γ N $\rightarrow$ η N $\rightarrow$ $\pi^o\pi^o\pi^o$N where the undetected part X is a pion plus a nucleon).

The initial nucleon is actually not at rest as it is part of a calcium nucleus so it has some Fermi momentum (the calcium nucleus is at rest but the nucleons forming the nucleus are not, they have around 150 MeV of momentum). This effect broadens the missing mass spectra. One can still use them, but good and background events are less well separated than for a hydrogen target where the nucleons have no Fermi momentum.

3.5.2 $\pi^o\pi^o$ selection

best pion combination

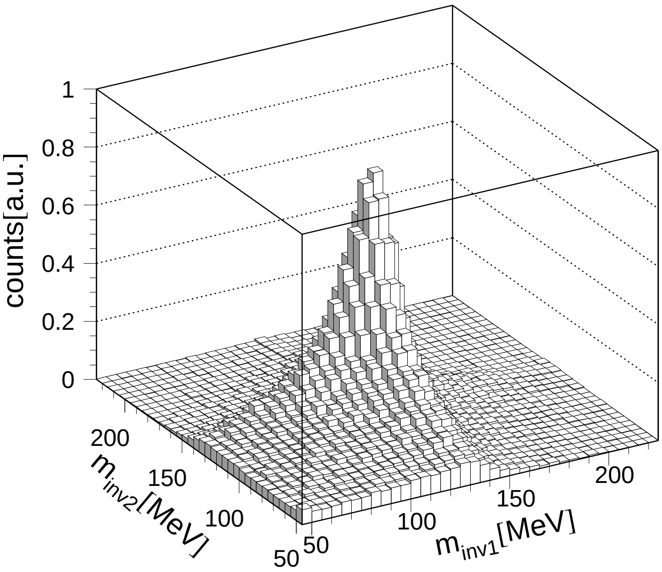

Figure 3.8: *Mass of photon pair 1 vs mass of photon pair 2 when 4 photons are detected. Events in the peak are* $\pi^o\pi^o$ *events.*

Each combination of 4 photons is studied $(\gamma_1\gamma_2, \gamma_3\gamma_4)$ and the masses of photon pairs are calculated (see figure 3.8). The masses $M_{\gamma_1\gamma_2}$ and $M_{\gamma_3\gamma_4}$ are checked to be close enough from the pion mass (between 100 and 150 MeV). If several combinations of the 4 photons fulfill this first condition, the right combination is choosen to be the one minimizing the expression:

$$\Delta M = \sqrt{(M_{\gamma_1\gamma_2} - M_{\pi^o})^2 + (M_{\gamma_3\gamma_4} - M_{\pi^o})^2} \tag{3.9}$$

It is called the “best pion combination”.

$\pi^o\pi^o$ missing mass

For the selected pion combination, the missing mass is calculated as explained in section 3.5.1. The mass of a nucleon is subtracted from the missing mass which makes “good events” centered at zero (see figure 3.9)

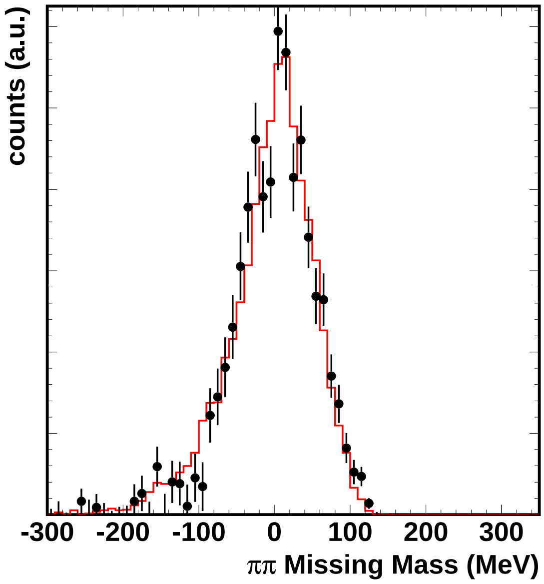

Figure 3.9: *$\pi^o\pi^o$ missing mass for incident photon energy in the range 400 to 500 MeV. In dots are the data points and the solid curve is simulated events.*

If the incident photon energy is large enough to produce an η -meson (around 600 MeV), background appears (2 pions detected out of a 3 pion decay of the eta which is very probable with 40% of 4π solid angle covered by the detectors). This background component gets larger when the η production cross section increases (see figure 3.10).

Due to the Fermi momentum of the initial nucleon, the missing mass peaks are broad and partly overlap (the true $\pi^o\pi^o$ events and the η background). If the accepted background quantity is minimized, the quantity of rejected good events increases. And vice-versa. A compromise has to be chosen knowing that the extra η background component, that is not cut out, can be subtracted as will be explained in the next chapter.

For a $\pi^o\pi^o$ event, the $\pi\pi$ missing mass is required to be in the range -100 to 100 MeV after subtraction of the nucleon mass. The same cut is applied to the simulation to correct this loss of $\pi\pi$ events with the detection efficiency. Some η events are not eliminated this way but their contribution to the cross section will be later estimated and subtracted.

3.5.3 $\pi^o\pi^+$ selection

The selection of $\pi^o\pi^+$ and $\pi^o\pi^-$ events is less easy than the one of $\pi^o\pi^o$ events. This is due to the properties of TAPS detector which is optimized for the detection of photons which makes it very efficient for the identification of neutral mesons.

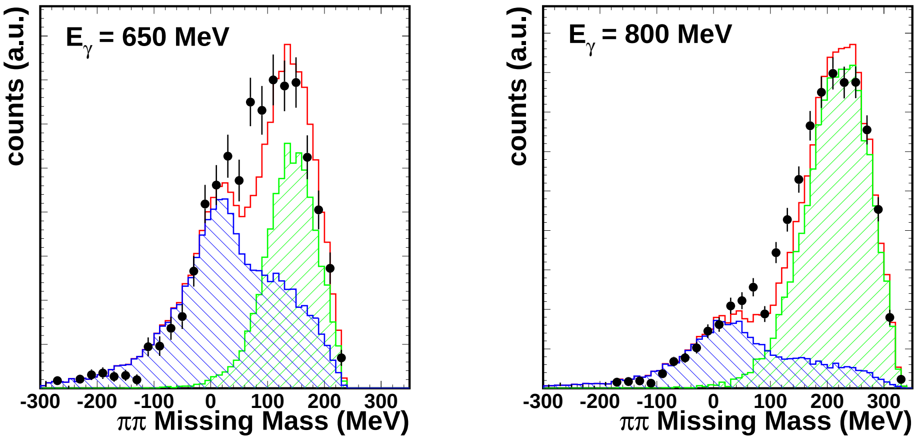

Figure 3.10: *$\pi^o\pi^o$ missing mass for incident photon energy of 650 MeV (left) and 800 MeV (right). The hatched area peaking at zero is a $\pi^o\pi^o$ simulation. The hatched area at larger missing mass is a $\eta \rightarrow 3\pi^o$ simulation. The third histogram is the sum of the two simulated components. The points are measured data. A $\pi\pi$ simulation is unable to reproduce the data and an η background component has to be added to get a good agreement with the data. The η component gets larger when the energy is larger as the η cross section rises faster than the $\pi^o\pi^o$ one in this energy range. The broad shape of the $\pi^o\pi^o$ contribution is due to the use of the final state interactions of the pions in the nucleus.*

Charged particles can also be detected and identified with some tricks as explained in section 3.4.
A $\pi^o\pi^\pm$ identification requires the following steps

- 2 photons are detected and fulfill the usual π^o conditions (mass and time coincidence)
- a charged particle is detected and fulfills $\pi^\pm$ conditions
- no other $\pi^\pm$ is detected to minimize background from ($\eta \rightarrow \pi^o\pi^+\pi^-$)
- the π^o missing mass for the (background) hypothesis (γN→π^op) with the proton mis-identified as π^+ is larger than 140 MeV

The π^o missing mass uses the same principle than the previous $\pi^o\pi^o$ missing mass but in the opposite way. Now the missing mass is calculated assuming the event is background. The mass of X is calculated in the channel (γN→π^oX). The detected charged pion is not used for this calculation. If the mass of the nucleon is subtracted from the mass of X, the missing mass ΔM_X is close to zero for an event (γN→π^op) where the charged particle identified as a pion is actually a proton. It

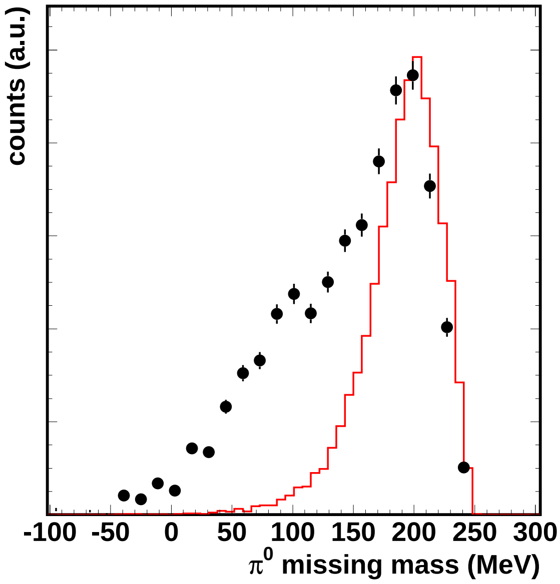

Figure 3.11: *π^o missing mass for an incident photon beam energy of E_γ = 400-460 MeV after substraction of the nucleon mass. The solid curve is a simulation of $\pi^o\pi^+$ events and the points are experimental data. Events with a π^o missing mass smaller than 140 MeV are assumed to be background events (with a proton miss-identified as a charged pion).*

sometimes happens as in the time-of-flight vs energy analysis, the "proton band" and the "$\pi^\pm$ band" partly overlap due to the large number of detected protons and some nuclear reactions which distorts the TOF vs energy signal. A "good event" (γN$\rightarrow\pi^o\pi^+$N) has a missing mass ΔM_X = M$_{\pi^+N}$ - M$_N$ different from zero and according to simulations ΔM_X mostly larger than 140 MeV (see figures 3.11 and 3.12). This background is important at low energy (near $2\pi^o$ production threshold) as the single pion cross section is large compared to the double pion cross section. It is not true at larger energy. Using a π^o missing mass cut (figures on the right) increases highly the agreement between data and simulation. Most $\pi^\pm$ candidates cutted away are very low energy. This is what is expected as most of the events cut out with the missing mass selection are in fact protons miss-identified as pions. These protons are slower than the pions in average (they are much heavier) so have a larger time of flight. Then, the kinetic energy calculated with the time of flight is smaller for protons miss-identified than for real pions. The absence of low energy $\pi^\pm$ compared to π^o comes from the analysis (selection of charged pions in the time-of-flight vs energy analysis).

It turned out that due to the high number of charged particles (mostly protons) detected in the forward wall, any event with the charged pions detected in this forward wall had to be rejected. The same condition is applied to the simulation

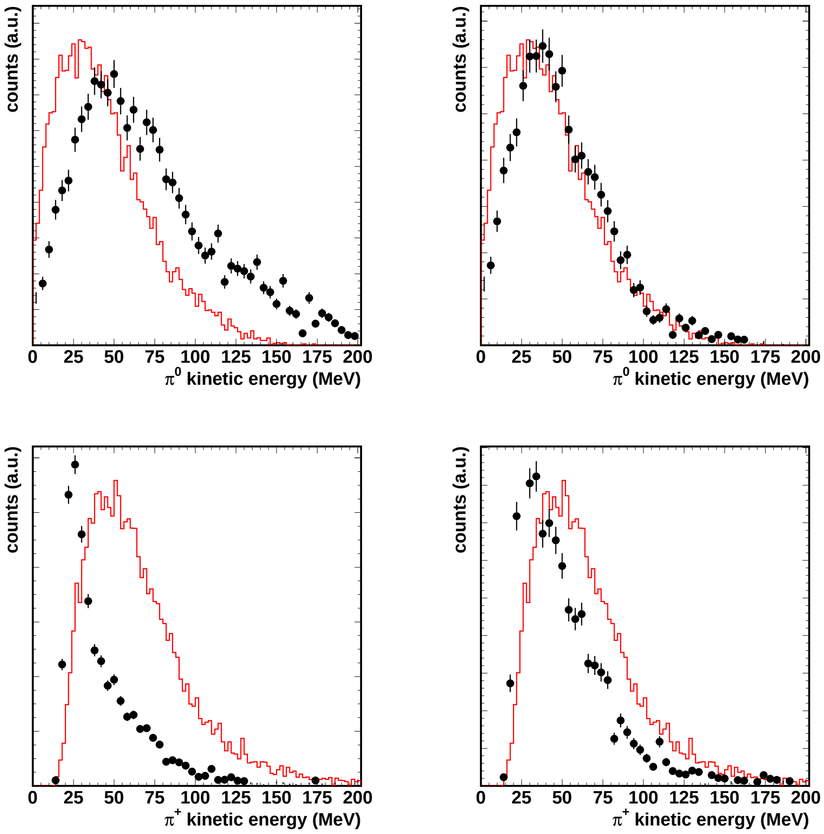

Figure 3.12: *The solid line is a simulation of* $\pi^o\pi^+$ *events and the points are the experimental data for an incident photon beam energy* E_γ *= 400-460 MeV. The two upper figures show the* π^o *kinetic energy with* π^o *missing mass cut (right) and without (left). The two lower figures show the* π^+ *kinetic energy with* π^o *missing mass cut (right) and without (left).*

during its analysis to calculate the detection efficiency which makes the cross section extrapolation possible as long as the angular distribution of $\pi^\pm$ are the same in the data and simulation.

3.5.4 $\pi^+\pi^-$ selection

Such events can't be studied with our setup. To be efficient we need to detect photons that can be used as a time reference. Other experiments including magnetic fields and more adapted detectors can study this channel (like CLAS).

Chapter 4

Cross section extraction

The previous part detailed how to select events of a given type (for this work, events where two pions are produced). It is possible to count them, but the extracted number depends highly on the setup and analysis.
What is needed are setup independent results which can be compared to other experiments and to theory predictions. This is called a cross section which is related to a probability for an incident photon to produce an event of the respective type.
The following sections will explain this absolute normalization.

4.1 Detection efficiency

The probability to reconstruct an event produced in the target is called the detection efficiency.

4.1.1 why a detection efficiency ?

Several reasons limitate the detection efficiency of $\pi\pi$ events:

- The detector does not cover the full solid angle but only 40% of it. At least one particle can easily reach none of the BaF_2 crystals.
- A minimal size of signals is required by the CFD and LED modules. A part of the signal or the whole signal can be missed if it happens to be below the thresholds.
- As detailed in the analysis part, identifying an event requires compromises. Increasing the chances to reject a bad event, increases also the chances to reject a good event. The analysis can this way reject good events and one has to estimate how often. e.g. cuts in TOF vs energy, $M_{\gamma\gamma}$, ...

4.1.2 principle

The detection efficiency is supposed to represent those effects. It is the probability to recognize an event of a certain type. This can depend on many variables as the incident photon energy or the detected particle angle or energy.
In order to get this value one needs to simulate the experiment as closely to the reality as possible. Then one can produce fake events and analyze them. But there, contrarily to the measured events, the events produced in the target are exactly known. The probability of detecting events which is the efficiency ε can be calculated:

$$\varepsilon = \frac{N_{analyzed}}{N_{start}} \tag{4.1}$$

Where N_{start} is the number of produced events and $N_{analyzed}$ is the number of reconstructed events.

4.2 Simulation

To produce a detection efficiency, one has to first simulate random events and then analyze them with exactly the same analysis that was used for the real data.

4.2.1 GEANT principle

The simulation of events was performed using the simulation package GEANT [51]. This set of programs simulates the interactions of particles with materials. The full setup of the experiment has to be precisely described including the targets, detectors and any piece of material that could lie on the path of particles. The type of events of interest is produced randomly (respecting all kinematical laws) and the produced particles are tracked through the detectors. All the interactions with the crossed materials are taken into account including also the natural decays of the particles. It is possible to produce particles decaying within the known branching ratio (like an η that can decay in 2 photons or 3 pions) or a fake particle (like an η decaying exclusively into $3\pi^o$ but having every other property of the usual η). So before GEANT tracks the particles during their flight, they have to be produced in the target with defined four-momenta. The following subsections will describe the used event generator.

4.2.2 $\pi^o\pi^o$

This generator produces 4 photons in the last step. The initial step is an incident photon of a given energy in the z-axis direction and a nucleon of a calcium nucleus at rest. Even when a nucleus is at rest, every of its nucleons has some momentum. The nucleus is at rest as the sum of the momenta of the nucleons is zero. This momentum called the Fermi motion has to be taken into account and is in the order of 100 MeV. A random Fermi momentum in a random direction is taken out of a given distribution (see fig. 4.1).

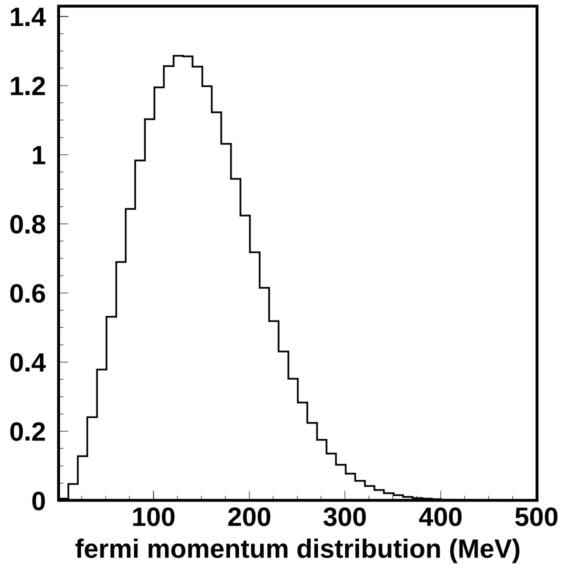

Figure 4.1: *Fermi momentum distribution of nucleons in the calcium nucleus used for the simulation of two pions events.*

The four-momenta of the incident photon and the target nucleon are added up and 3 particles (two of the mass of the π^o and one of the proton mass) are produced like phase space in the center of momentum with the routine GENBOD2 of GEANT (the sum of the four-momenta is first checked to be large enough to produce those three particles). GENBOD generates a multi-particle weighted event according to Lorentz-invariant Fermi phase space using the method of Raubold and Lynch [52]. The produced particles are after that boosted to the lab frame. The π^o are produced in the nucleus. They first need to escape it. They suffer from final state interactions (FSI). The nucleus is represented by a parameter related to its radius. The π^o is moved step by step of a random distance taken out of its mean free path distribution and as long as its still inside the nucleus it gets for each step an interaction with a nucleon of the nucleus. The radius parameter (in arbitrary unit) is used to make fit the missing mass distribution of simulation to the data.

Then, for each of these two π^o after they escaped the nucleus, the same routine GENBOD2 is used to produce two photons. The final state is then a nucleon and 4 photons. They are "given" to GEANT that can track them and give an output of the same kind as for one of real measured events.

4.2.3 $\pi^o\pi^\pm$

This generator is exactly the same as the $\pi^o\pi^o$ except that one of the three produced particles has the mass of a charged pion instead of the mass of a π^o. Once a nucleon, a π^o and a π^+ are produced, the π^o decays into two photons like in the previous generator and the π^+ is given directly to GEANT to be tracked. The charged pion can be either a π^+ or a π^-.

The charged pions suffer from the same FSI as the neutral pions.

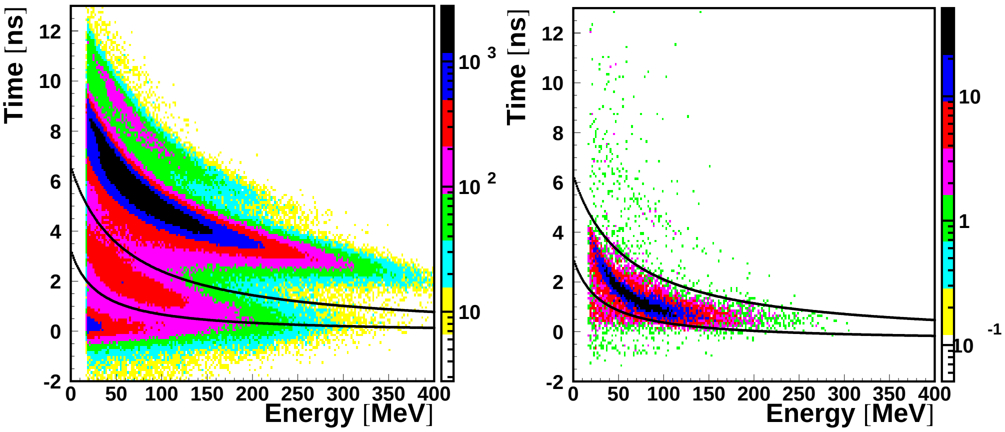

Figure 4.2: *Time-of-flight versus deposited energy of charged particles (logarithmic scale). Particles between the two curves are identified as charged pions. Left is data (many protons or other particles are visible) and right is simulation (almost every particle is a π^+).*

A specific problem was introduced with the π^+ simulation. While the π^- get absorbed by nuclei after they deposited their energy, the π^+ decay into anti-muons after $\Delta t_{\pi^+} = 2.6\times10^{-8}$ s. Once the anti-muons deposited their small energy, they are trapped and decay after some micro seconds ($\Delta t_\mu = 2.2\times10^{-6}$ s) into electron. This muons decay in the experiment after the electronics gates are closed. So no trace of the deposited energy from the muon decay products exist in the data. This is not the default case of the simulation. It was then needed to stop the tracking of particles in the simulation after a while (5×10^{-7} s). Only with this specification it was possible to get rid of extra deposited energy and extra detectors hits in π^+ clusters.

4.2.4 η

The η cross section is needed to subtract some background from the $\pi\pi$ production. As the η can decay into three pions, if we detect only two of them, this event which is actually a η event can be miss-identified as a 2 pions event. Much of them can be removed with a missing mass analysis, but not all of them. One has to estimate this contribution and to subtract it from the cross section. In order to do that, one has first to measure the η cross section and then to estimate the part of it which is miss-identified as a 2 pion event. The η decays at 39.43 % into 2γ, at 32.51 % in $3\pi^o$ and at 22.6 % in $\pi^o\pi^+\pi^-$. These three channels are produced.

$\eta \rightarrow \gamma\gamma$ is used to measure the η cross section, and the three-pion channels are used to calculate the background on the 2 pion events.

4.2.5 $\eta \rightarrow \gamma\gamma$

The safer way to calculate the η cross section is to measure its 2γ decay channel. It's really easy to identify and done the same way as a π^o identification. The missing mass spectra of 2 photons shows a clear peak at the η mass, see fig. 3.5.

This event generator is a bit different than the others as the detection efficiency depends highly on the energy and angle of the eta. The start distribution of events in this channel is flat in θ and energy. The produced efficiency is applied individually to each detected η.

4.2.6 $\eta \rightarrow \pi\pi\pi$

Such an event is produced in a way close to the $\pi\pi$ events.

The η is first produced out of the photon-nucleon pair like phase space and the η is given to GEANT asked to only decay into 3 pions. The simulation has to be weighted with the branching ratio $\eta \rightarrow \pi\pi\pi$.

Depending on the reaction used, the pion triplet can either be $\pi^o\pi^o\pi^o$ (when studying $\pi^o\pi^o$ production) or $\pi^o\pi^+\pi^-$ (when studying $\pi^o\pi^+$ production).

The pions don't suffer from FSI as the η meson decays out of the nucleus. The η escaping the nuclear medium are almost not distorted by FSI. Pions can be several times absorbed and re-emitted by the Δ resonance, but η mesons which are absorbed are rarely reemitted (no more than 10% of the observed η's have been at least once absorbed and reemitted). And since the η cross section was measured from 2 photons, this already includes η FSI.

4.3 number of incident photons

To get a cross section one needs to know how many photons impinged on the target and produced the measured number of events. This is needed to normalize the number of counts.

4.3.1 scalers

The scalers are electronic modules counting the number of detected electrons in the tagger. The electron tagger is an 100% efficient detector, so for each produced photon in the radiator, one count is added to the scalers.

4.3.2 Tagging efficiency

The relevant number is the number of photons hitting the target and not the number of photons produced (which is the number of electrons detected in the tagger and called the scalers). The number of photons hitting the target is smaller than the number of photons produced in the radiator. The photons are produced via bremsstrahlung in a narrow forward cone. But in order to have a small enough beam hitting the target, a collimator is used to collimate the beam. This collimator stops the less forward photons. A tagging efficiency can be produced and used to correct the scalers which is defined the following way :

$$\varepsilon_{tagger} = \frac{N_\gamma}{N_{e^-}} \tag{4.2}$$

where N_γ is the number of photons hitting the target and N_{e^-} the number of photons produced in the radiator (ie the number of detected electrons in the tagger).

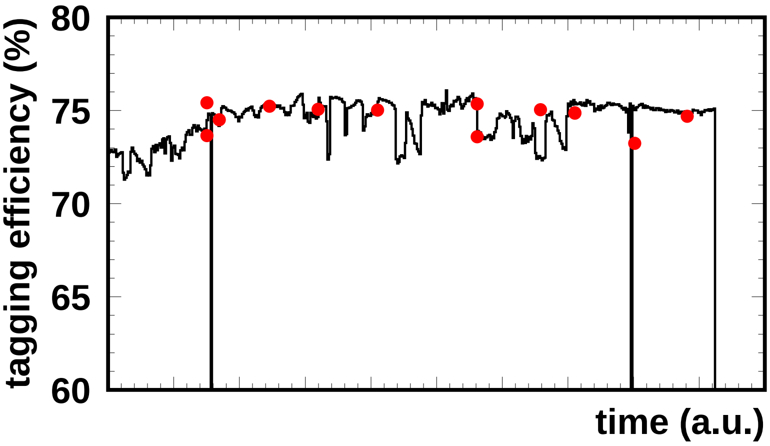

Figure 4.3: *Average tagging efficiency tracked over the whole experiment as derived from the count rates in the photon counter P2 (solid line) absolutely scaled to the single measurements of the tagging efficiency (points).*

During the experiment N_γ is not known but to measure this efficiency an extra detector is used. It is a 100% efficient photon detector which is put directly in the beam line after the target. This detector can't stand the large photon flux so separated runs are made several times during the experiment with a much smaller photon flux. The detector is moved into the beam line only during these "tagging efficiency runs". The efficiency can now be measured as function of the tagger channel as the ratio between the number of photons detected in the tagging efficiency detector and the number of electrons detected.

The tagging efficiency is not a constant over time as can be checked with the different tagging efficiency measurements. This variation is mainly due to the instability of the beam as its position or width can slightly change over time.

The variations can be measured using a proportional counter standing in the end of the beam-line during the whole experiment. We don't get an absolute number of detected photons but its relative variations. The count rate of this detector P2 divided by the counts in the tagger N_{e^-} is proportional to the tagging efficiency.

$$\varepsilon_{tagger} \sim \frac{P2}{N_{e^-}} \tag{4.3}$$

This time dependent curve is adjusted to the real tagging efficiency measurement and is used to calculate an average tagging efficiency over the whole experiment. This efficiency can now be used to correct the scalers into the number of photons hitting the target.

4.4 Coincidence analysis

4.4.1 Problem

The aim of an experiment is to accumulate a lot of statistics in a short time as beam-time is very money consuming. The more intense our beam is, the more events we can produce. And especially as only a very small fraction of the incident photons interact with the target, the electron beam (producing photons via bremsstrahlung as described in the chapter on the setup) has to be used with a high intensity. The tagger detecting every electron that produced a photon, for one event produced in the target (ie particles detected in TAPS), more than ten electrons in average are detected in the electron-tagger as can be seen in the tagger multiplicity figure 4.4.

Each of these electrons produced a bremsstrahlung photon, but only one of those photons interacted with the target and induced the detected particles. The aim of the tagger is to determine the energy of the photon that produced a detected event. We have now to find out which of these ten electrons produced the photon that induced the event. Each combination of the event detected in TAPS with every electron is treated as a different event.

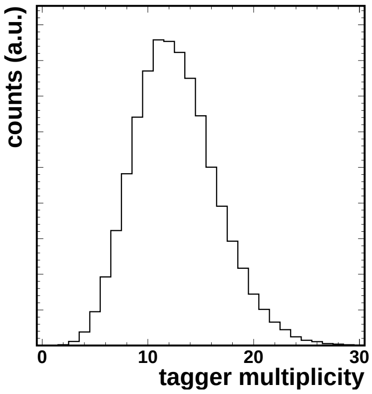

Figure 4.4: *Tagger multiplicity ie number of electrons detected in the tagger in a time range of 150 ns around a* $\pi\pi$ *event.*

4.4.2 Principle

For each event, the time difference between the particles detected in TAPS and the electron detected in the tagger associated to this event is measured, (see figure 4.5).

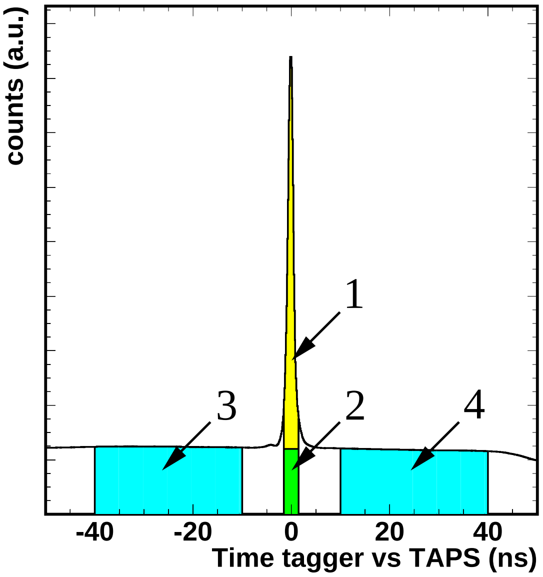

Figure 4.5: *Time difference between an electron in the tagger and a photon detected by TAPS.*

This time distribution shows a peak at time zero (this value comes from the time calibration as explained in the chapter on data analysis) and a large constant plateau.

Two different regions can be selected. Region 1+2 is called coincident event as the electron and the particles are detected in time coincidence, and the region 3+4 is called random background events.

The coincident events can be of two kind. The region 1 which are the true coincident events, and the region 2 which are accidental coincidence.

Region 2, 3 and 4 are all part of this large plateau coming from events where the electron associated to the detected particles is not related to them. For such events, the electron and the particles are uncorrelated and can have any time difference with the particles, and even (like in region 2) be accidentally in time coincidence with them.

We can select events with a time coincidence, to remove most of the plateau background. But the accidental coincidence (region 2) are also selected this way and there is no way to decide if one event belongs to region 1 or 2 (real or accidental coincidence).

Those "bad" events cannot be cut out but need to be subtracted to get meaningful distributions.

4.4.3 Solution

The background subtraction is possible due to the nature of the plateau. For such background events, the electron associated to the particles, is uncorelated to them. This means that at any time difference between the electron and the particles, the same amount of background can be found which is clear from the flat shape of the plateau (see figure 4.5). The background is also of the same kind for any time difference.

So any distribution measured for coincident events is made up of a component of real coincident events (region 1 of figure 4.5) plus a component of accidental coincident events (region 2) which needs to be subtracted. And the component of accidental coincident events is the same that would be the contribution for any other background events. And this component can be measured selecting only background events (regions 3 and 4).

To get smaller statistical uncertainties, the background region is chosen as large as possible and on both side of the peak to average any fluctuation of the plateau. To get the same component to a given distribution from the background events and the accidental coincident events, the background events need to be weighted to make the region 2 and the region 3+4 have the same area. Coincident events are defined as events with a time difference between the electron and the particles between -1.5 and 1.5 ns. The background events are defined as having a time difference between -40 and -10 ns (region 3) OR between 10 and 40 ns (region 4). The background events have then to count as 0.05 of an event to normalize the areas : $\frac{(1.5-(-1.5))}{(-10-(-40))+(40-10)} = 0.05$.

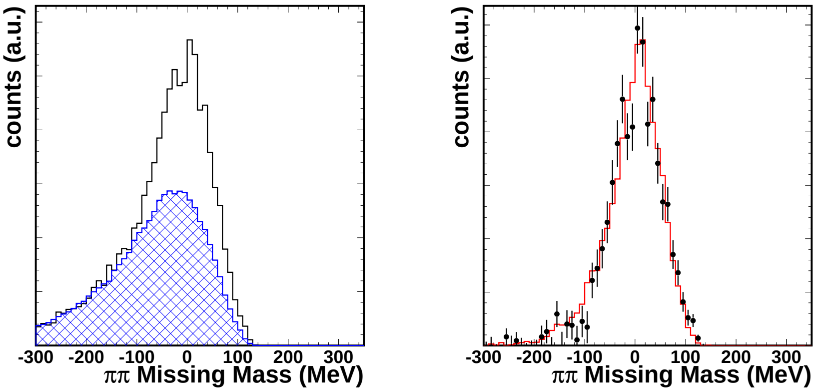

Figure 4.6: *These plots show the* $\pi^o\pi^o$ *missing mass (in MeV) of the data for incident photon energy between 400 and 500 MeV. On the left hand side, the hatched area corresponds to random background events, while the other histogram is the coincident events. The right hand side plot (solid dots) shows the difference of the two previous histograms. The histogram is a simulation of* $\pi^o\pi^o$ *events. The simulation fits very nicely with the data after the random background subtraction.*

For a given distribution D, the contribution D_1 of the region 1 is the relevant information. With a selection of coincident events (time difference between -1.5 and 1.5 ns), the contribution of coincident events D_{co} is measured which is the sum of contribution D_1 of region 1 and D_2 of region 2. With a selection of background events, after the weighting of the events, the contribution of the background D_{bg} is obtained which is the sum of contributions D_3 and D_4 of regions 3 and 4.
The wanted contribution can be calculated:

$$D_1 = D_{co} - D_2 = D_{co} - D_{bg} \tag{4.4}$$

as

$$D_{bg} = D_3 + D_4 = D_2 \tag{4.5}$$

This can be applied to a missing mass distribution (see chapter on the data analysis for more details) as shown in figure 4.6. The contribution of background events is the hatched area on the left. The contribution of coincident events is defined by the other histogram on the left. The subtraction of these two components (area between the two left curves) is shown as the dots on the right and this is the contribution of the real coincident events. The efficiency of this method can be checked by the comparison between the data after background subtraction and simulated events (solid curve on the right) where this background does not exist (in the simulation, every incident photon produces an event).
Another example is shown with the $\pi^o\pi^o$ count rate in figure 4.7.
Note that in tagging efficiency measurements such background does not exist, as the intensity of the beam is much smaller.

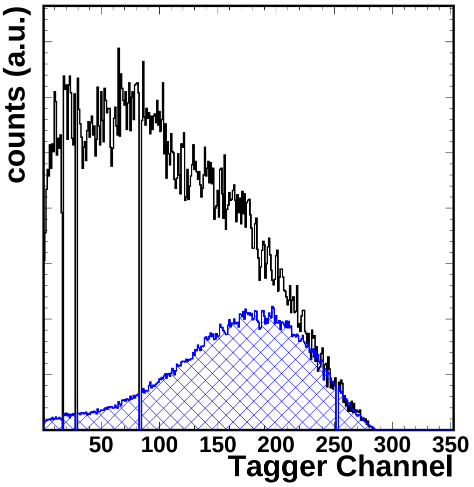

Figure 4.7: $\pi^o\pi^o$ *count rate versus the tagger channel (smaller tagger channel corresponds to higher incident photon energy). The upper curve corresponds to the coincident events and the lower hatched curve is the random background. The correct counting rate after random background subtraction is the area between the two curves. Subtracting the background cuts out unrealistic events like two pions produced below the threshold (which is around tagger channel 220 on calcium).*

4.5 Cross section calculation

4.5.1 total cross section

The total cross section is defined the following way.

$$\sigma_{tot}(E_\gamma) = \frac{N_{event}(E_\gamma)}{\varepsilon_{taps}(E_\gamma) \cdot \Gamma_{br} \cdot N_{target} \cdot N_\gamma(E_\gamma)} \tag{4.6}$$

where :

- $N_{event}(E_\gamma)$ is the number of reconstructed events of the kind studied ($\pi\pi$).
- $\varepsilon_{taps}(E_\gamma)$ is the detection efficiency calculated with simulations (see figure 4.8)
- Γ_{br} is the branching ratio of the measured channel.

  For $\pi^o\pi^o$,

  $$\Gamma_{br} = \Gamma_{2\pi^o\to 4\gamma} = (\Gamma_{\pi^o\to\gamma\gamma})^2 = 0.988^2 \tag{4.7}$$

  For $\pi^o\pi^+$ events,

  $$\Gamma_{br} = \Gamma_{\pi^o\pi^+\to\gamma\gamma\pi^+} = \Gamma_{\pi^o\to\gamma\gamma} = 0.988 \tag{4.8}$$

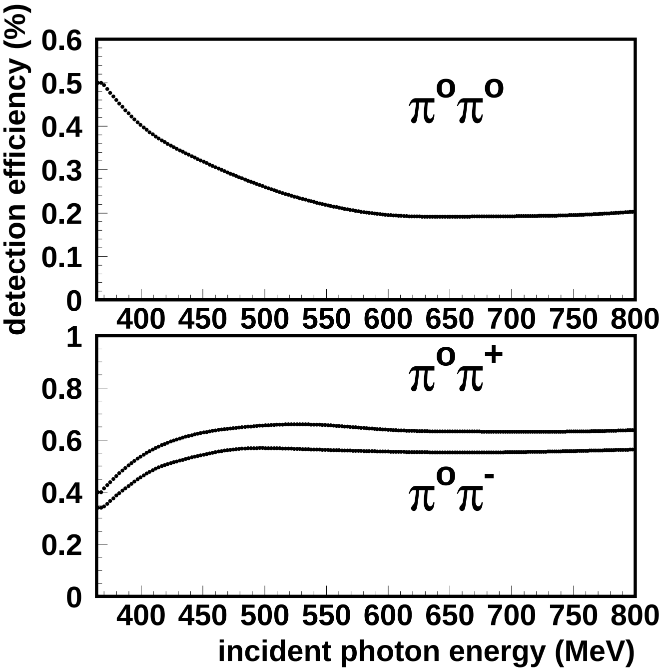

Figure 4.8: *$\pi\pi$ detection efficiency as a function of the incident photon energy. In addition to the shape difference in the threshold region, one can notice the larger average efficiency for $\pi^o\pi^+$ and $\pi^o\pi^-$ than for $\pi^o\pi^o$ which can be mainly explained by the fact that a $\pi^\pm$ is directly detected but a π^o is detected via its two photon decay, so a $\pi^o\pi^o$ event requires four detected particle versus three for a $\pi^o\pi^+$ event (and the detectors cover a third of the full solid angle). The drop at low energy of the efficiency in the $\pi^o\pi^\pm$ channel must partly come from our reconstruction of charged pions which requires a minimum pion energy. For the $\pi^o\pi^\pm$ channel, the efficiency used to correct the data is the average of $\pi^o\pi^+$ and $\pi^o\pi^-$ efficiencies.*

- N_{target} is the number of Ca nuclei targets per cm^2 (or barn).

$$N_{target} = \frac{\mathcal{N}_A \cdot \rho_{Ca} \cdot L_{target}}{M_{Ca}} \tag{4.9}$$

with $\mathcal{N}_A$ the Avogadro number, ρ_{Ca} the calcium density, L_{target} the target thickness and M_{Ca} the molar mass of calcium.

$$N_{target} = \frac{6.022 \cdot 10^{23}(mol^{-1}) \cdot 1.54(g.cm^{-3}) \cdot 0.9907(cm)}{40.08(g.mol^{-1})} = 2.29 \cdot 10^{22} cm^{-2} \tag{4.10}$$

- $N_\gamma(E_\gamma)$ is the number of incident photons hitting the target.

$$N_\gamma(E_\gamma) = scalers(E_\gamma) \cdot \varepsilon_{tagging}(E_\gamma) \tag{4.11}$$

where the scalers are the number of electrons detected in the electron tagger and $\varepsilon_{tagging}$ the tagging efficiency (probability for a bremsstrahlung photon produced in the radiator to reach the target).

η cross section

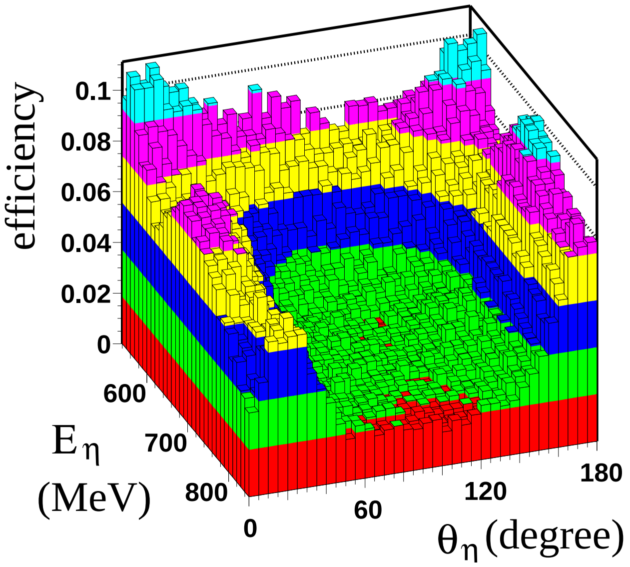

Figure 4.9: η *meson detection efficiency in its two-photon decay as function of its angle* (θ_η) *and total energy* (E_η)*. No detection holes are present (the minimum efficiency is around 2%).*

The η cross section is needed to subtract the events where an η meson is produced in the target, it decays into 3 pions ($\pi^o\pi^o\pi^o$ or $\pi^o\pi^+\pi^-$) and only 2 of these 3 pions are detected. Most of these events can be eliminated via a missing mass analysis but not all of them. This contribution needs to be subtracted. Two elements have to be known: the η cross section and in a second step we want to know the probability for an η decaying into 3π to be missidentified as a $\pi\pi$ event. The η cross section is measured in its $\eta \rightarrow \gamma\gamma$ channel. These events are identified with an invariant mass analysis of photon pairs in the same way as π^o are identified. The invariant mass of the photon pair is asked to be in the range 500-600 MeV.

The detection efficiency is applied during the analysis on an event-by-event basis to each reconstructed η depending on its kinetic energy and angle. This detection

efficiency calculated with an $\eta \rightarrow \gamma\gamma$ simulation is applied as a weight for the reconstructed event (see figure 4.9).
The cross section is calculated the same way as the $\pi\pi$ one with $N_{event}/\varepsilon_{taps}$ replaced by the sum of the weights of all reconstructed η-mesons. The branching ratio $\eta \rightarrow \gamma\gamma$ is $\Gamma_{br} = 39.43\%$.

$\pi\pi$ cross section

The $\pi\pi$ total cross section can be measured but contains a component from η background. Most of those η can be recognize in the analysis with the missing mass analysis like in the case of a $\eta \rightarrow \pi\pi\pi$ event where two of the three pions are detected, the missing mass can be everything and will be a broad distribution which is different from the mass of a nucleon. Selecting the events this way implies to choose a limit. If this limit is strict, most η will be removed but many true $\pi\pi$ events too. If the cut is less stringent, less $\pi\pi$ events will be rejected but much more η will need to be subtracted. A compromise is chosen to keep events with a missing mass between -100 and 100 MeV. The η background component represents here around 20% of the $\pi\pi$ cross section. With a missing mass selection of -100 to 200 MeV, the η component would represent 70% of the measured $\pi\pi$ cross section. Subtracting such a large component would bring too large errors to the final cross section. The result has to be the same for every accepted missing mass range as the detection efficiency takes also into account this -more or less- strict event selection. But the stricter the cut is, the more the result is depending on how well the simulation reproduces the data distributions.
This has been checked with a combination of a $\pi\pi$ and $\eta \rightarrow \pi\pi\pi$ simulations (see figure 3.10).
The $\pi\pi$ cross section is defined as :

$$\sigma_{\pi\pi}(E_\gamma) = \sigma_{\pi\pi,measured}(E_\gamma) - \sigma_\eta(E_\gamma) \cdot \varepsilon_{\eta\rightarrow(\pi\pi)\pi} \cdot \Gamma_{\eta\rightarrow 3\pi} \tag{4.12}$$

with $\varepsilon_{\eta\rightarrow(\pi\pi)\pi}$ the efficiency to reconstruct an $\eta \rightarrow \pi\pi\pi$ event as a $\pi\pi$ event and $\Gamma_{\eta\rightarrow 3\pi}$ the branching ratio $\eta \rightarrow 3\pi$ (32.51% for $\pi^o\pi^o\pi^o$ and 22.6% for $\pi^o\pi^+\pi^-$). These quantities are multiplied to the η cross section as the smaller they are, the less produced η will look like $\pi\pi$ events.
The $\pi^o\pi^\pm$ efficiency is more tricky to determinate than the $\pi^o\pi^o$ one. This is due to the charged pions analysis specificities (tof-vs-energy cut, $\pi^\pm$ required out of the forward-wall, ...). However it can be nicely checked with the $\eta \rightarrow \pi^o\pi^+\pi^-$ reaction.

4.5.2 Invariant mass distributions of the pion pairs

Apart from the total $\pi\pi$ cross section, the invariant mass of the pion pairs is studied, which has the information on possible in-medium effects of the σ-meson. For a given energy range, the mass of the pion pairs is given as a differential cross section $\frac{d\sigma}{dM_{\pi\pi}}$. The mass of the pion pair is calculated as the square of the sum of the four-momenta of the two pions, the same way that the pions are identified with the mass of the photon pairs.

As the statistics are not good enough to produce the invariant mass for every tagger channel (small bin of incident photon energy of 1 to 2 MeV), it is necessary to use larger intervals of incident photon energy and the the differential cross section will be an average over this energy range.

The $\pi\pi$ mass distribution are measured in both channels $\pi^o\pi^o$ and $\pi^o\pi^+$ for the two following energy ranges : E_γ = 400-500 MeV (close to the production threshold) and E_γ = 500-550 MeV (which is still below the η production threshold, so free of η background).

The simulation needs to reproduce the data as the detection efficiency is not constant over the full energy range. The number of events produced in the simulation to calculate the efficiency has to depend on the incident photon energy. This dependence is given by the measured total cross section.

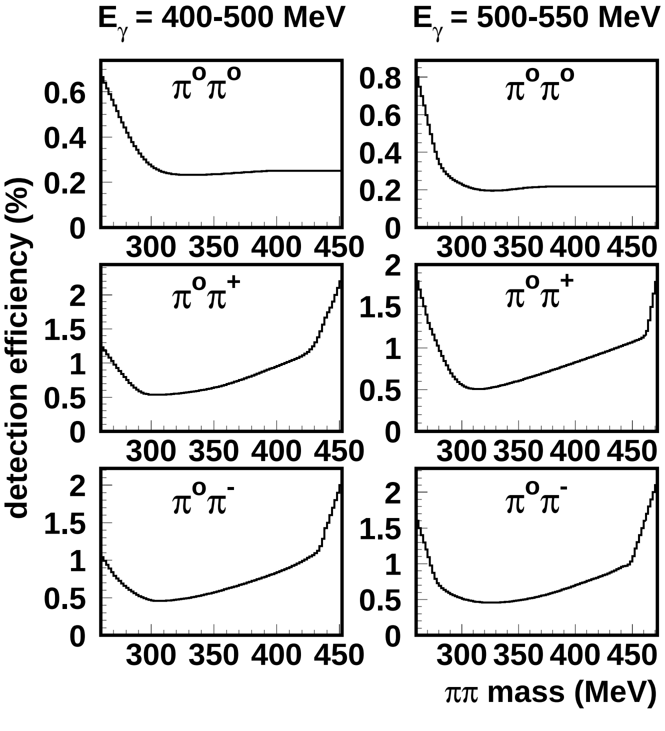

Figure 4.10: $\pi\pi$ *detection efficiency as a function of the 2 neutral pions mass for the two incident photon energy ranges.*

Calculated efficiency is shown in fig. 4.10. For each energy range, the efficiency is produced in the three isospin channels $\pi^o\pi^o$, $\pi^o\pi^+$ and $\pi^o\pi^-$. The efficiency used to correct $\pi^o\pi^\pm$ mass distribution is an average of $\pi^o\pi^+$ and $\pi^o\pi^-$ efficiencies. The main difference in the shape of $\pi^o\pi^o$ and $\pi^o\pi^\pm$ efficiencies is the behavior at large two pion invariant mass. $\pi^o\pi^o$ efficiency is almost constant while $\pi^o\pi^\pm$ efficiencies increase with increasing $M_{\pi\pi}$. The sharp increase of the $\pi^o\pi^\pm$ efficiencies at large two pion mass is an extrapolation of the detection efficiency as very few events are simulated in this region which is at the border of the available phase-space.

Chapter 5

Results and discussion

5.1 total cross section

5.1.1 η-production

The total η cross section has been extracted from the $\eta \to \gamma\gamma$ decay channel. It is compared in fig. 5.1 to a fit of the results of previous experiments [21, 22, 23, 54].

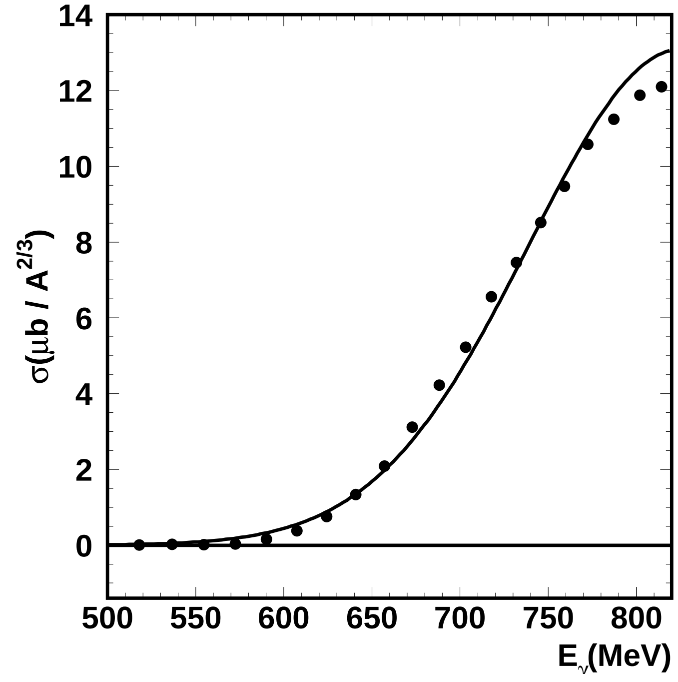

Figure 5.1: *Measured η total cross section in the $\eta \to \gamma\gamma$ channel. The solid line is a fit of published data [21]. The slight disagreement around 800 MeV comes from the fit limitations. For a more precise comparison, see [21].*

The agreement is very good and limits systematic uncertainites from the overall normalization of the data and from the detection and reconstruction of photons.

Furthermore, in order to investigate systematic effects in the detection efficiency of charged pions, the eta excitation function has also been extracted from the $\eta \rightarrow \pi^o \pi^+ \pi^-$ decay channel (see fig. 5.2).

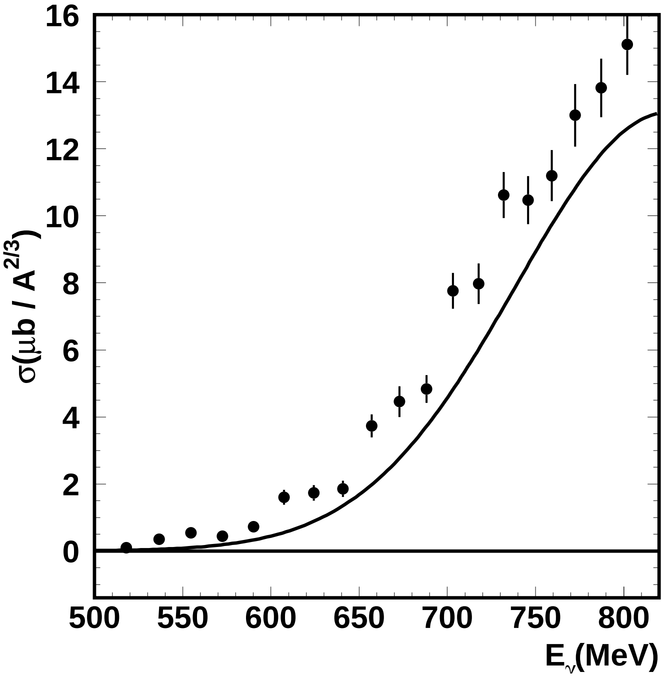

Figure 5.2: *Measured η total cross section in the $\eta \rightarrow \pi^o \pi^+ \pi^-$ channel. The solid line is a fit of published data [21].*

For this channel the same $\pi^o \pi^\pm$ analysis has been used as for the extraction of the double pion cross section, but an additional charged pion was required with the same identification cuts as for the first charged pion. The result agrees within 15% with the eta cross section from the two-photon channel, which is somewhat overestimated. This is expected since in the eta invariant mass distribution (see fig. 3.7) from this channel a small background component from triple pion production not originating from eta decays is visisble. Altogether this comparisons limits the systematic uncertainty for the detection and identification of charged pions (which enters squared into it) at the 10% level.

The η total cross section measurement in the two presented channels is good check for the photon and charged pions analysis that should not suffer from any important systematic reconstruction error.

5.1.2 $\pi^o\pi^o$

The total $\pi^o\pi^o$ production cross section has been measured, as explained in the previous part, with the TAPS detectors on a calcium target. In figure 5.3 and 5.4, it is represented as a function of the incident photon energy.

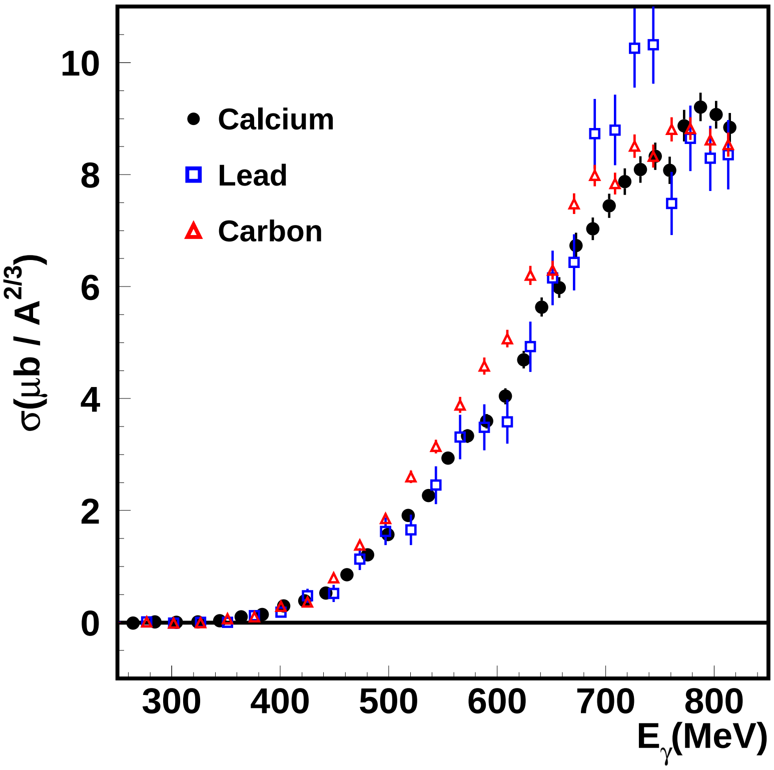

Figure 5.3: *Total $\pi^o\pi^o$ production cross section as a function of the incident photon energy on different nuclei. The cross sections are normalized like $A^{2/3}$. Carbon and lead data by S. Schadmand [53] are preliminary.*

In order to get informations on the medium influence, it is compared to the same cross section on other targets (carbon and lead fig. 5.3, and deuterium fig. 5.4). The normalization used is the atomic number to the power 2/3 ($A^{2/3}$) for nuclei with A>2 and a factor of 2 for the deuteron.

With this normalization the cross sections from the different nuclei agree almost perfectly within their statistical uncertainties. It was already discussed in [21, 22, 23], that such a scaling holds for all so far investigated exclusive meson production reactions in the second resonance region. The scaling of the cross sections of the heavier nuclei with $A^{2/3}$ is what is expected when only the nuclear surface contributes to the reactions, and thus an indication for strong final state interaction. The agreement with the average nucleon cross section (that is half the deuteron cross section) has been found phenomenologically.

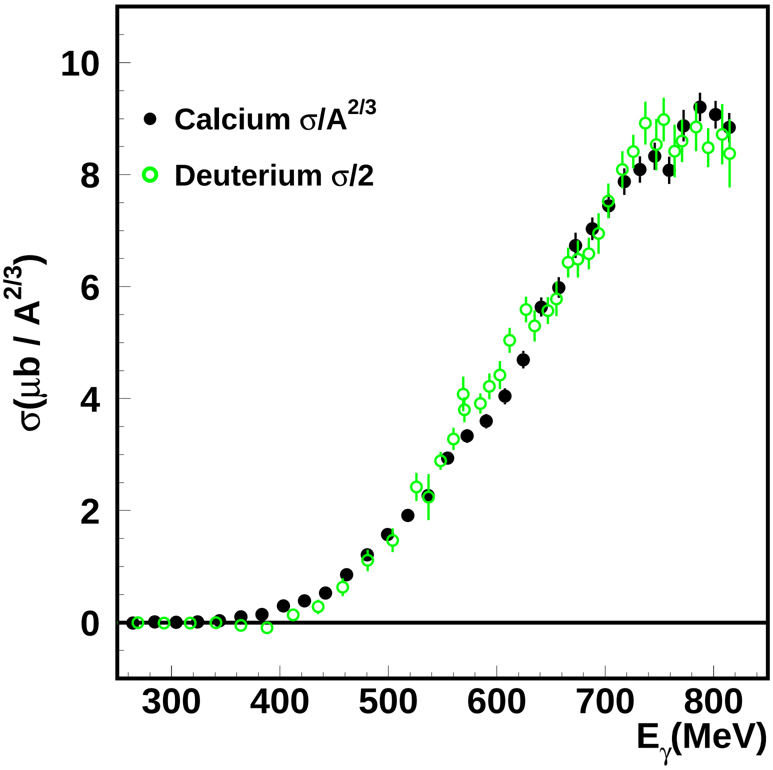

Figure 5.4: *Total $\pi^o\pi^o$ production cross section as a function of the incident photon energy on calcium and deuterium. For the normalization, see text.*

As the photons can scan, with the same probability, the center of the nuclei and its surface (which is not the case with a pion beam for instance), it could mean both that the production of neutral pion pairs is much less probable at higher density (the nuclear density inside the nucleus is larger than in the surface), or that the pions produced deeply inside the nuclei are not detected. The latter is the most probable solution since it is known that pions with momenta large enough to excite the Δ resonance undergo strong final state interactions. They have a high probability of beeing absorbed in the nucleus and if only one pion from the pair is removed (e.g. via the ΔN→NN collisonal channel) the reaction is not any more identified as double pion production.
Exept this absorptive FSI no in-medium modifications have been found in this channel, in particular as discussed above, the shape of the excitation functions follows almost exactly the average of the free proton/neutron cross sections, showing no indication for a suppression of the second resonance bump.

5.1.3 $\pi^o\pi^\pm$

The $\pi^o\pi^\pm$ production cross section is shown in figures 5.5 and 5.6. This cross section is the sum of the $\pi^o\pi^+$ and $\pi^o\pi^-$ cross sections, since the setup used for these measurements contains no magnetic field and can't discriminate between positively and negatively charged particles.

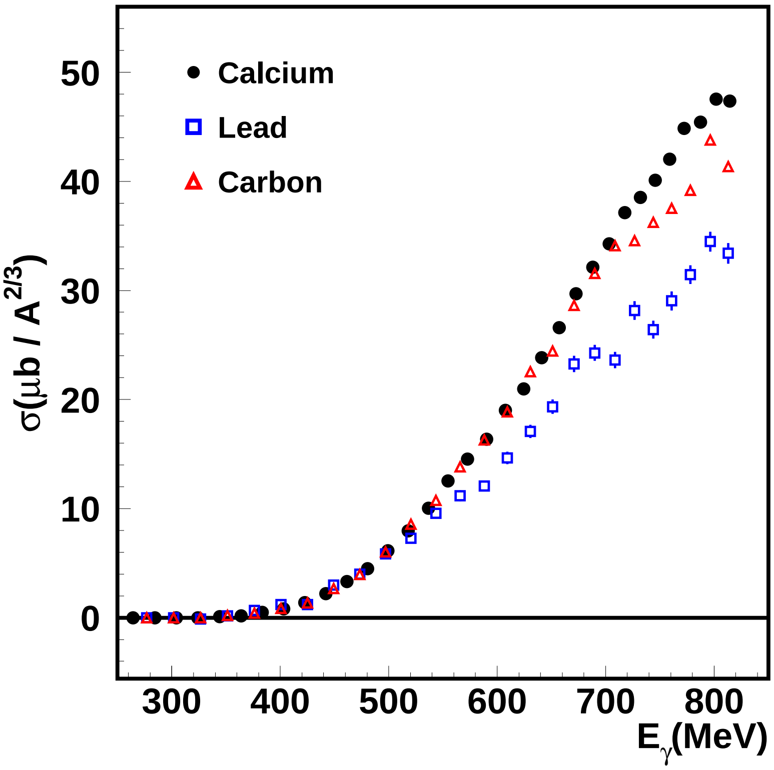

Figure 5.5: *Total* $\pi^o\pi^\pm$ *production cross section as a function of the incident photon energy on different nuclei. The cross sections are normalized like* $A^{2/3}$. *Carbon and lead data by S. Schadmand [53] are preliminary.*

When scaled by $A^{2/3}$, the cross sections for calcium and carbon agree but the cross section for lead is significantly smaller (see figure 5.5). Lead and carbon data are preliminary. The unexpected difference between lead and other nuclei must be confirmed by further analysis.

The different behavior for lead would be somewhat surprising since there is no tendency to a suppression of the cross section from carbon to calcium. Furthermore, this would be a completely different behavior as was observed for the neutral pion pairs. One might of course speculate that the mixed charge channel could be more sensitive to medium modifications due to the contribution of the rho-meson [32] which is forbidden for the neutral channel. As discussed in [32], in-medium effects on the rho spectral function could modify the width of the D_{13} resonance resulting in a suppressed resonance structure in the D_{13} range. However, the analysis of the lead data in view of systematic detection efficiency effects etc. is not yet final. Therefore, here we can only state that no unexpected in-medium effects are observed in the comparison of the carbon and calcium data.

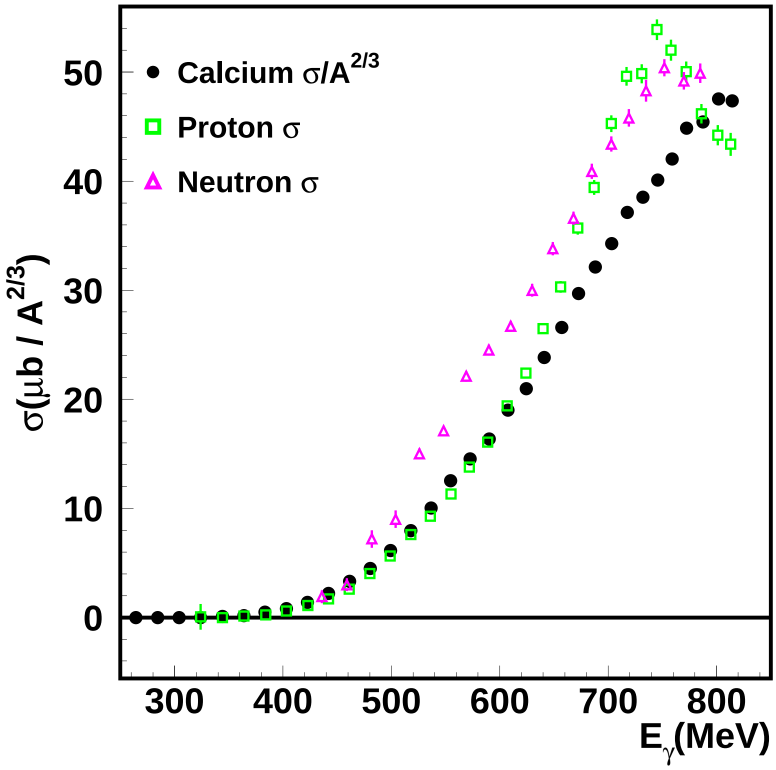

Figure 5.6: *Total* $\pi^o\pi^\pm$ *production cross section as a function of the incident photon energy on calcium (normalized by* $A^{2/3}$*) compared to proton and neutron.*

When scaled to $A^{2/3}$ these data agree within their systematic uncertainties on the order of 10 - 15 %. The statistical uncertainties are negligible and much smaller than for the $\pi^o\pi^o$ channel. This is so because the cross section is larger and only three hits (two photons, one charged pion) have to be detected so that the geometrical detection efficiency is larger.

The cross section is also compared to the free proton and quasifree neutron cross section as shown in figure 5.6. Also this comparison seems to indicate the absence of a large in-medium suppression of the resonance structure, although the agreement is not as good as for the double π^o channel (compare figure 5.4).

5.2 $\pi\pi$ mass

The extraction of invariant mass distributions of the pion pairs was one of the main goals of this work. Such distributions have been produced for the $\pi^o\pi^o$ and the $\pi^o\pi^\pm$ channels (fig. 5.7 and 5.8).

Two energy ranges (400 to 500 MeV and 500 to 550 MeV) have been chosen in order to have enough statistics to produce meaningful distributions and also to get an information on the influence of the incident photon energy. The two

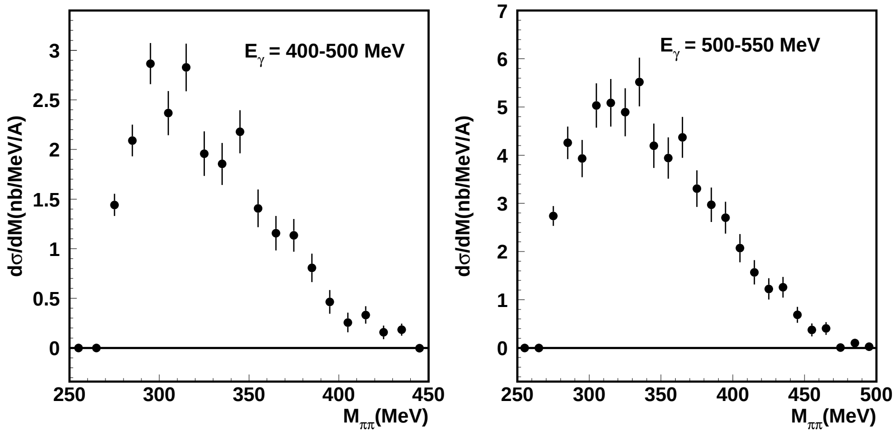

Figure 5.7: *$\pi^o\pi^o$mass distribution for incident photon energy in the range 400-500 MeV (left) and 500-550 MeV (right) normalized by A (40 for calcium).*

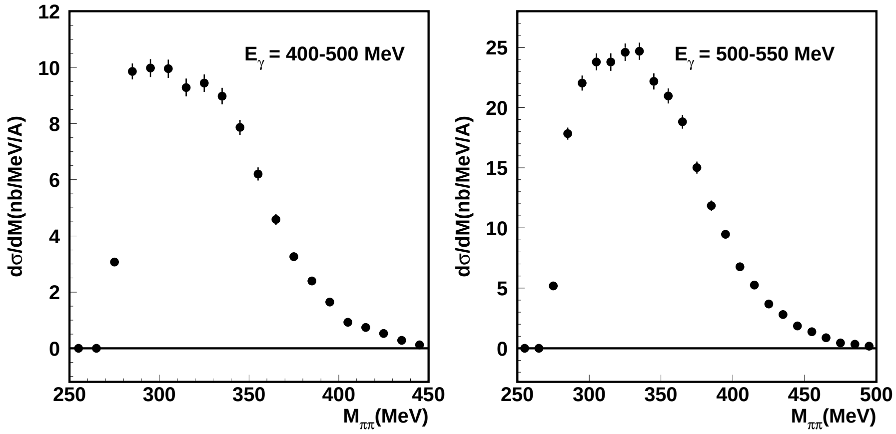

Figure 5.8: *$\pi^o\pi^\pm$mass distribution for incident photon energy in the range 400-500 MeV (left) and 500-550 MeV (right) normalized by A (40 for calcium).*

energy ranges have been chosen below the η meson production threshold (around E_γ= 600 MeV) to avoid background from this source.

The comparison between the two channels can give valuable information on the in-medium behavior of the σ-meson. If σ-mesons have been produced and can be detected in their two pion decay, the mass of the two pions would be the mass of the σ. Models suggest a decrease of the sigma mass with with increasing density so that it becomes degenerate with its chiral partner, the pion, at large density.

In this case a shift of the strength in the invariant mass distributions towards small values is expected for the double π^o channel, but not for the $\pi^o\pi^\pm$ channel, where the σ cannot contribute. Such effects can be searched for in the spectra in two ways. One can compare the shape of the $\pi^o\pi^o$ and $\pi^o\pi^\pm$ spectra for each nucleus and one can compare the evolution of the $\pi^o\pi^o$ and $\pi^o\pi^\pm$ spectra as function of mass number. The latter is done by normalizing the Ca and Pb spectra to carbon.

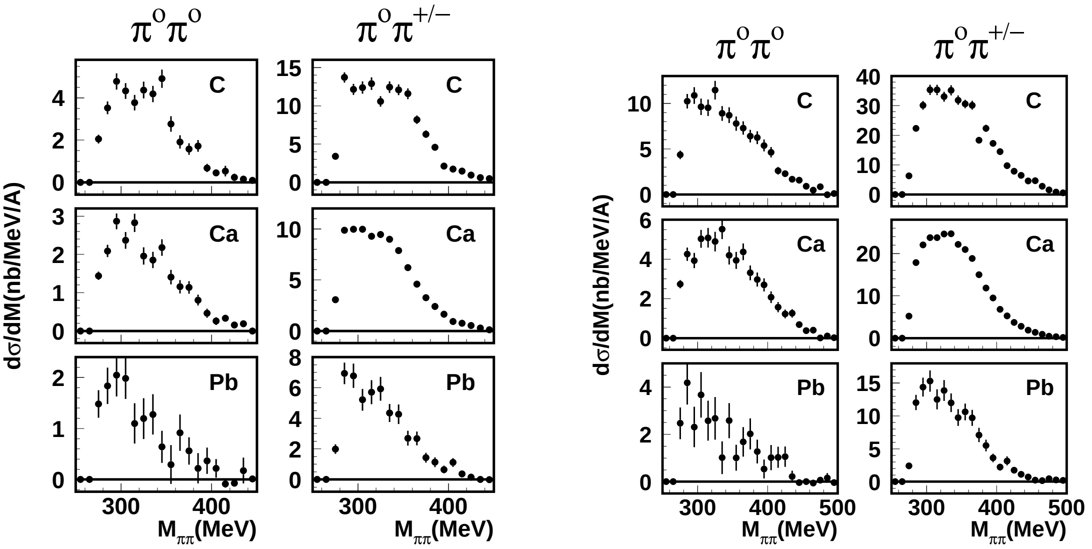

Figure 5.9: *Comparison of the invariant masses of the pion pairs for different target nuclei (C, Ca, Pb) normalized by A for an incident photon energy in the range 400 to 500 MeV (left panel) and 500 to 550 MeV (right panel). In each panel, left: $\pi^o\pi^o$, right: $\pi^o\pi^\pm$. The results for carbon and lead (S. Schadmand [53]) are preliminary.*

The $\pi\pi$ invariant mass for different targets (carbon, calcium and lead) is shown in figure 5.9. These three targets allow to scan over increasing nuclear density (from carbon to lead). Data on lead and carbon are preliminary.

A comparison of the invariant mass distributions for different nuclear density is shown in figure 5.10 for both energy ranges as a ratio of the differential cross sections from different targets (Ca/C and Pb/C). The solid lines indicate the result of a linear fit to the data. The ratios of the $\pi^o\pi^o$ and $\pi^o\pi^\pm$ invariant mass distributions are summarized in figure 5.11.

The $\pi^o\pi^o$ invariant mass distributions from the lead target normalized to carbon show the behavior that was already previously reported in [16], i.e. a clear rize to small invariant masses. However, the reanalysed $\pi^o\pi^\pm$ data show also some increase to small invariant masses. In the new Ca data almost no rise to small invariant masses is observed for the neutral channel, but unexpectedly some rise of the ratio at small invariant masses is seen for the mixed charge channel. One should, however, keep in mind that the carbon data which has been used for normalization is still preliminary. An independent cross section is the comparison of the $\pi^o\pi^o$ and $\pi^o\pi^\pm$ distributions in fig 5.11.

These ratios are almost constant for carbon and calcium in both ranges of incident photon energy. Only for lead some rise to small invariant masses appears for the lower range of incident photon energies. This is, however, at the limit of statistical

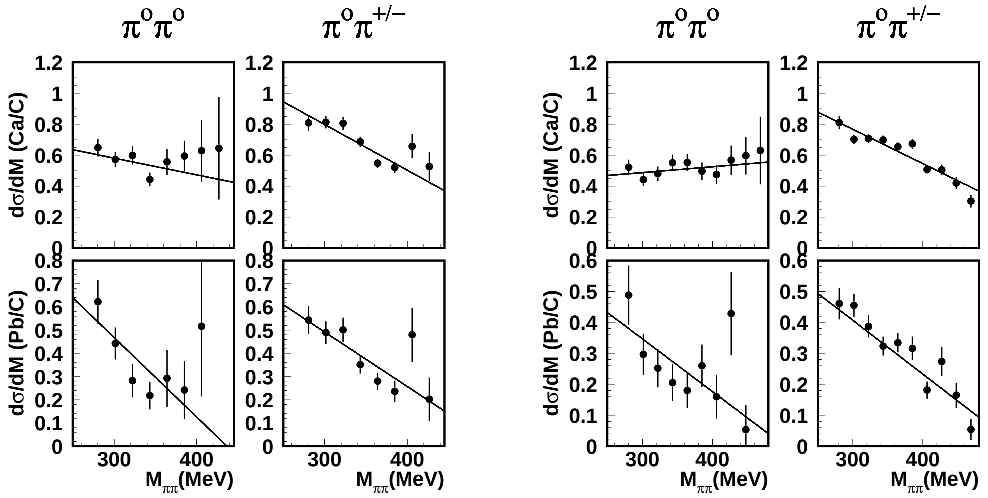

Figure 5.10: *Ratio of the differential cross sections. Left panel is for an incident photon beam energy of 400 to 500 MeV and right panel 500 to 550 MeV. For each panel, the $\pi\pi$ mass ratio is shown for calcium/carbon (up) and lead/carbon (down) and for both $\pi^o\pi^o$ and $\pi^o\pi^\pm$. The solid lines are linear fits of the data points.*

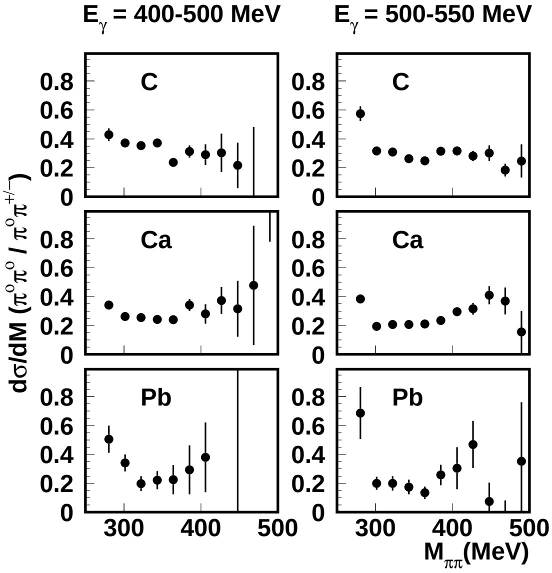

Figure 5.11: *Ratios of the $\pi^o\pi^o$ and $\pi^o\pi^\pm$ invariant mass distributions on the three targets for an incident photon beam energy of 400 to 500 MeV (left) and 500 to 550 MeV (right).*

significance. In summary, there are no significant effects seen in the Ca spectra, which could point to an in-medium modification of the σ mass. This is somewhat surprising since the results which have been reported from pion induced double π production [14] show very similar effects for Ca and Pb.

Some more analysis is still needed on the lead and carbon data to compare them accurately with the calcium distributions shown in this work.

5.3 comparison with theory

5.3.1 the BUU-model

Many references [57, 58] describe in details the BUU transport model. This section will focus on the basic ideas.

The model is based on the BUU (Boltzmann-Uehling-Uhlenbeck) equation which describes the space-time evolution (r: space coordinate, p: momentum) of the spectral phase-space density F_i of an ensemble of interacting particles of type $i = N, \Delta(1232), \pi, \eta, ...$ with mass μ:

$$(\frac{\delta}{\delta t} + \bigtriangledown_p H \cdot \bigtriangledown_r - \bigtriangledown_r H \cdot \bigtriangledown_p) F_i(r, p, \mu; t) = I_{coll}[F_N, F_\pi, F_{\Delta(1232)}, F_\eta, ...] \quad (5.1)$$

The left-hand side -the Vlasov term- describes the propagation of the particles under the influence of a Hamilton function H, given by the expression

$$H = \sqrt{(\mu + S)^2 + p^2}, \quad (5.2)$$

which in the case of baryons contains an effective scalar potential S [58]. The right-hand side of the BUU equation (called the collision integral) consists of a gain and a loss term for the phase space density F_i at the different space-time points, accounting for interactions between the particles beyond the mean-field potential. The collision integral contains collision rates for the different reaction types such as baryon-baryon and baryon-meson collisons, resonance formation and decay. They include cross sections for these processes and Pauli blocking factors for outgoing fermions.

For the description of a system of non-identical particles one gets an equation for each particle species that is coupled to all others by the collision integral or the mean-field potential.

5.3.2 comparison

Figures 5.12 and 5.13 show a comparison between data from this work and the results of calculations in the framework of the BUU model [56, 55].

The top part in both pictures shows the total cross section and bottom part the double π invariant mass distributions for the two ranges of incident photon energies.

The $\pi^o\pi^o$ data are quite well reproduced by the model 5.12. Only in the lower energy region a slight shift to smaller masses of the measured distribution with

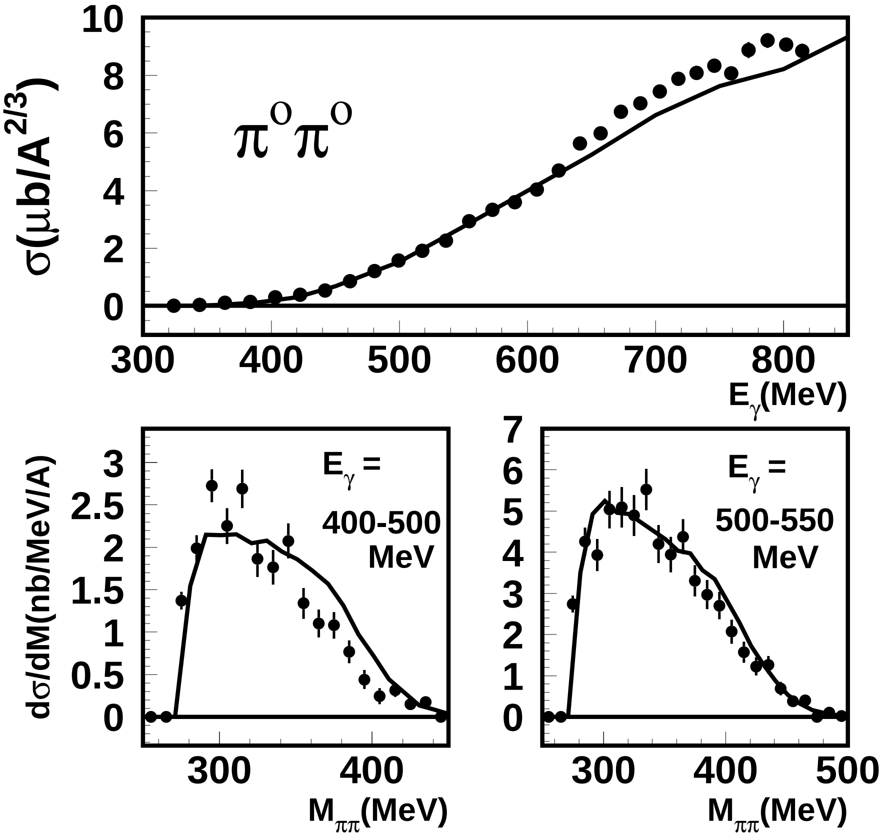

Figure 5.12: *Calcium $\pi^o\pi^o$ data (solid points) compared to theory by Pascal Muelich [55] (curve). Up is total cross section and down $\pi\pi$ mass for two different incident photon energy range.*

respect to the model results is seen, in the second energy range the data are almost exactly reproduced. Also the total cross section is very well reproduced. Only for the highest energies it is slightly underestimated. However, one has to keep in mind that in this energy region the data have a larger systematic error (on the order of 10%) due to the subtraction of the background from missidentified eta decays. Summarizing, the BUU model calculations, which do not include any effects from chiral symmetry restoration, reproduce the data suprisingly well.
The case of the $\pi^o\pi^{\pm}$ channel is somewhat different 5.13. The total cross section in the threshold region is overestimated by the model calculations. Howerver, also in this case the invariant mass distributions when scaled in the absolute normalization describe the data reasonably well.

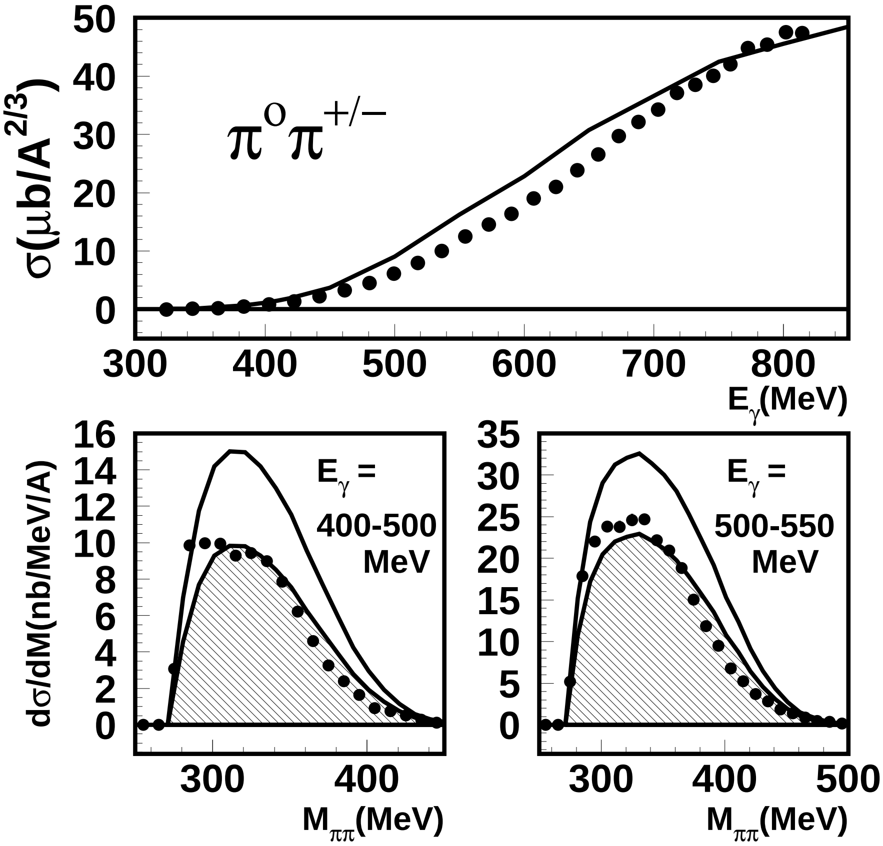

Figure 5.13: *Calcium $\pi^o\pi^\pm$ data (solid points) compared to theory by Pascal Muelich [55] (curve). The hatched area is the curve normalized to the data. Up is total cross section and down $\pi\pi$ mass for two different incident photon energy range.*

Chapter 6

Conclusions and outlook

The total $\pi\pi$ photoproduction cross section has been measured in both $\pi^o\pi^o$ and $\pi^o\pi^\pm$ channels. A better understanding of the in-medium behavior of the second resonance bump was expected.
Both channels show strong final state interaction effects. Total cross sections agree for nuclei when scaled with $A^{2/3}$. This is the signature that only the surface of nuclei contributes to the cross sections. Since the probes are real photons, the full nuclei are illuminated with the same probability. Double pions events produced in the center must then suffer from very strong FSI.
In the $\pi^o\pi^o$ channel, absolutely no surprising suppression of the bump structure of the second resonance region is found. In the $\pi^o\pi^\pm$ channel, there could be a small effect which needs to be checked in a deeper analysis of other targets data. But nothing is seen that would show a strong in-medium effect on the D_{13} e.g. due to its ρ coupling.
In addition, both channels agree quite well with the BUU model, so there is no indication for non-understood effects.

Invariant mass distributions of pion pairs have been also measured to find indications on a possible partial restoration of the chiral symmetry. A signature would be a shift of $\pi^o\pi^o$ invariant mass distribution toward small masses at large density that would not be visible in $\pi^o\pi^\pm$. Contrarily to the CHAOS collaboration results, no effect indicating an in-medium modification of the σ-meson is seen in the data taken by TAPS detectors between carbon and calcium. But a shift to low mass is still visible between the light nuclei (C and Ca) and lead.
Every measured invariant mass distributions are in reasonable agreement with the BUU calculations.

The data on lead and carbon -beeing still preliminary- need some further analysis to confirm the above discussed results.

The TAPS detectors are since 2004 back at the MAMI accelerator where a set of experiments are made together with the Crystal Ball detector. This configuration provides a geometrical acceptance close to 4π. New data with very high statistics can be expected for solid targets that will allow to deepen the subjects studied in this work.

Chapter 7

Appendix

7.1 Units

The units used in this work are the ones usually used in nuclear physics. The energy unit is the electron Volt (eV) and its multiples, the KeV (Kilo electron Volt = 10^3 eV) and the MeV (Mega electron Volt = 10^6 eV). 1 eV is equal to $1.6022.10^{-19}$ J.

Momentum and mass are also given in eV that actually represent respectively eV/c and eV/c^2 as the two main constants are taken by convention c = 1 (speed of light) and $\hbar = 1$ (Planck's constant).

The momentum $\vec{p}$ and the total energy are usually combined in four-vectors.

$$p = \begin{pmatrix} p_0 \\ p_1 \\ p_2 \\ p_3 \end{pmatrix} = \begin{pmatrix} E \\ \vec{p} \end{pmatrix} \tag{7.1}$$

7.2 Tables

7.2.1 Tagger energy calibration

channel	E_γ(MeV)	ΔE_γ(MeV)
1	818.91	1.17
2	817.71	1.20
3	816.46	1.25
4	815.17	1.30
5	813.83	1.35
6	812.43	1.40
7	810.99	1.45
8	809.49	1.51
9	807.94	1.55
10	806.34	1.60
11	804.69	1.65
12	803.00	1.69
13	801.26	1.73
14	799.49	1.76
15	797.68	1.80
16	795.84	1.82
17	793.98	1.85
18	792.09	1.87
19	790.19	1.88
20	788.28	1.89
21	786.36	1.89
22	784.45	1.89
23	782.54	1.87
24	780.65	1.86
25	778.78	1.84
26	776.94	1.81
27	775.12	1.78
28	773.34	1.75
29	771.59	1.71
30	769.87	1.68
31	768.17	1.67
32	766.49	1.62
33	764.88	1.58
34	763.24	1.61
35	761.61	1.62
36	759.98	1.63
37	758.33	1.64
38	756.68	1.65
39	755.02	1.65
40	753.35	1.65
41	751.68	1.64
42	749.99	1.64
43	748.31	1.63
44	746.62	1.63
45	744.92	1.63
46	743.22	1.62
47	741.51	1.62
48	739.77	1.66
49	738.05	1.66
50	736.32	1.65
51	734.61	1.70
52	732.87	1.69
53	731.12	1.69
54	729.37	1.69
55	727.61	1.68
56	725.83	1.72
57	724.06	1.71
58	722.28	1.71
59	720.51	1.75

channel	E_γ(MeV)	ΔE_γ(MeV)
60	718.72	1.75
61	716.93	1.74
62	715.12	1.74
63	713.31	1.74
64	711.50	1.73
65	709.68	1.73
66	707.85	1.73
67	705.99	1.77
68	704.15	1.77
69	702.30	1.77
70	700.47	1.81
71	698.61	1.81
72	696.74	1.80
73	694.87	1.80
74	692.99	1.80
75	691.10	1.79
76	689.19	1.83
77	687.29	1.83
78	685.38	1.83
79	683.49	1.86
80	681.57	1.86
81	679.65	1.86
82	677.72	1.85
83	675.78	1.85
84	673.84	1.85
85	671.87	1.89
86	669.91	1.88
87	667.95	1.88
88	666.00	1.92
89	664.03	1.92
90	662.05	1.91
91	660.06	1.91
92	658.07	1.91
93	656.07	1.90
94	654.05	1.94
95	652.03	1.93
96	650.02	1.93
97	648.01	1.96
98	645.98	1.96
99	643.95	1.96

channel	E_γ(MeV)	ΔE_γ(MeV)
100	641.91	1.95
101	639.86	1.95
102	637.81	1.94
103	635.73	1.99
104	633.66	1.98
105	631.59	1.98
106	629.54	2.02
107	627.46	2.02
108	625.37	2.01
109	623.28	2.01
110	621.18	2.00
111	619.08	2.00
112	616.97	1.99
113	614.83	2.03
114	612.71	2.03
115	610.59	2.02
116	608.48	2.06
117	606.34	2.05
118	604.20	2.05
119	602.05	2.04
120	599.90	2.04
121	597.74	2.03
122	595.58	2.03
123	593.38	2.07
124	591.21	2.07
125	589.03	2.06
126	586.87	2.11
127	584.68	2.10
128	582.49	2.10
129	580.29	2.09
130	578.09	2.09
131	575.88	2.08
132	573.67	2.07
133	571.42	2.12
134	569.20	2.12
135	566.97	2.11
136	564.77	2.16
137	562.53	2.15
138	560.29	2.15
139	558.05	2.14

channel	E_γ(MeV)	ΔE_γ(MeV)
140	555.80	2.13
141	553.54	2.13
142	551.28	2.12
143	549.02	2.11
144	546.72	2.16
145	544.45	2.16
146	542.18	2.15
147	539.92	2.20
148	537.64	2.19
149	535.35	2.19
150	533.06	2.18
151	530.76	2.17
152	528.46	2.16
153	526.16	2.16
154	523.85	2.15
155	521.51	2.20
156	519.19	2.19
157	516.87	2.19
158	514.58	2.24
159	512.25	2.23
160	509.92	2.22
161	507.58	2.21
162	505.24	2.21
163	502.90	2.20
164	500.56	2.19
165	498.21	2.18
166	495.83	2.24
167	493.47	2.23
168	491.11	2.22
169	488.78	2.27
170	486.42	2.27
171	484.05	2.26
172	481.68	2.25
173	479.30	2.24
174	476.92	2.23
175	474.54	2.22
176	472.16	2.22
177	469.75	2.26
178	467.36	2.25
179	464.96	2.24
180	462.60	2.29
181	460.20	2.28
182	457.80	2.27
183	455.40	2.26
184	452.99	2.26
185	450.58	2.25
186	448.17	2.24
187	445.76	2.23
188	443.31	2.28
189	440.89	2.28
190	438.47	2.27
191	436.08	2.32
192	433.66	2.31
193	431.23	2.30
194	428.80	2.30
195	426.37	2.29
196	423.93	2.28
197	421.50	2.27
198	419.06	2.26
199	416.62	2.25
200	414.15	2.30
201	411.71	2.29
202	409.26	2.28
203	406.84	2.33
204	404.39	2.32
205	401.94	2.30
206	399.49	2.30
207	397.04	2.28
208	394.58	2.28
209	392.12	2.26
210	389.67	2.25
211	387.21	2.24
212	384.71	2.30
213	382.24	2.29
214	379.78	2.28
215	377.35	2.35
216	374.88	2.33
217	372.42	2.32
218	369.95	2.31
219	367.48	2.30

channel	E_γ(MeV)	ΔE_γ(MeV)
220	365.00	2.29
221	362.53	2.28
222	360.06	2.27
223	357.58	2.26
224	355.07	2.32
225	352.59	2.31
226	350.11	2.30
227	347.67	2.36
228	345.19	2.35
229	342.71	2.34
230	340.23	2.33
231	337.75	2.32
232	335.27	2.31
233	332.78	2.30
234	330.30	2.29
235	327.82	2.27
236	325.30	2.33
237	322.81	2.32
238	320.33	2.31
239	317.87	2.36
240	315.39	2.35
241	312.90	2.34
242	310.41	2.33
243	307.93	2.31
244	305.44	2.30
245	302.95	2.29
246	300.46	2.28
247	297.97	2.27
248	295.45	2.32
249	292.96	2.31
250	290.47	2.30
251	288.02	2.36
252	285.53	2.34
253	283.04	2.33
254	280.55	2.32
255	278.06	2.31
256	275.57	2.30
257	273.09	2.29
258	270.60	2.27
259	268.11	2.26

channel	E_γ(MeV)	ΔE_γ(MeV)
260	265.59	2.32
261	263.10	2.31
262	260.61	2.29
263	258.16	2.35
264	255.67	2.34
265	253.19	2.33
266	250.70	2.32
267	248.22	2.30
268	245.73	2.29
269	243.25	2.28
270	240.76	2.27
271	238.28	2.26
272	235.77	2.30
273	233.29	2.29
274	230.81	2.28
275	228.36	2.33
276	225.88	2.31
277	223.40	2.30
278	220.92	2.29
279	218.44	2.28
280	215.97	2.26
281	213.49	2.25
282	211.01	2.24
283	208.54	2.23
284	206.03	2.29
285	203.56	2.28
286	201.09	2.26
287	198.65	2.32
288	196.18	2.31
289	193.72	2.30
290	191.25	2.29
291	188.78	2.27
292	186.32	2.26
293	183.85	2.25
294	181.39	2.24
295	178.93	2.23
296	176.44	2.27
297	173.98	2.26
298	171.52	2.25
299	169.10	2.30

channel	E_γ(MeV)	ΔE_γ(MeV)
300	166.64	2.29
301	164.19	2.27
302	161.73	2.26
303	159.28	2.25
304	156.83	2.24
305	154.38	2.23
306	151.94	2.21
307	149.49	2.20
308	147.02	2.25
309	144.57	2.24
310	142.13	2.23
311	139.72	2.28
312	137.28	2.26
313	134.85	2.25
314	132.41	2.24
315	129.98	2.23
316	127.55	2.22
317	125.12	2.20
318	122.69	2.19
319	120.26	2.18
320	117.84	2.17
321	115.38	2.22
322	112.96	2.20
323	110.54	2.19
324	108.15	2.24
325	105.73	2.23
326	103.32	2.22
327	100.91	2.21
328	98.49	2.20
329	96.08	2.18
330	93.68	2.17
331	91.27	2.16
332	88.87	2.15
333	86.46	2.13
334	84.03	2.19
335	81.63	2.17
336	79.24	2.16
337	76.87	2.21
338	74.48	2.20
339	72.09	2.19
340	69.70	2.18
341	67.31	2.17
342	64.93	2.15
343	62.55	2.14
344	60.17	2.13
345	57.79	2.12
346	55.41	2.10
347	53.00	2.16
348	50.63	2.15
349	48.26	2.14
350	45.93	2.19
351	43.56	2.18
352	41.10	2.36

7.2.2 $\pi^o\pi^o$ total cross section

E_γ(MeV)	σ (μb)
814.38	103.40 ± 3.07
802.03	106.09 ± 2.90
787.32	107.69 ± 2.97
772.54	103.79 ± 3.31
759.14	94.45 ± 2.86
745.76	97.40 ± 2.86
731.98	94.62 ± 2.75
717.81	92.12 ± 2.78
703.23	87.06 ± 2.50
688.24	82.23 ± 2.38
672.84	78.79 ± 2.64
657.05	69.98 ± 2.13
640.87	65.89 ± 2.01
624.31	54.90 ± 1.83
607.39	47.29 ± 1.68
590.13	42.06 ± 1.52
572.54	38.96 ± 1.40
554.66	34.31 ± 1.26
536.48	26.53 ± 1.10
518.04	22.40 ± 0.97
499.37	18.40 ± 0.85
480.49	14.15 ± 0.73
461.39	9.96 ± 0.61
442.12	6.17 ± 0.50
422.71	4.53 ± 0.42
403.16	3.50 ± 0.34
383.50	1.66 ± 0.26
363.76	1.22 ± 0.21
343.95	0.35 ± 0.17
324.08	0.10 ± 0.15

7.2.3 $\pi^o\pi^\pm$ total cross section

E_γ	σ (μb)
814.38	553.94 ± 4.94
802.03	556.00 ± 4.58
787.32	531.24 ± 4.48
772.54	524.66 ± 4.93
759.14	491.73 ± 4.22
745.76	468.91 ± 4.06
731.98	450.56 ± 3.85
717.81	434.46 ± 3.84
703.23	400.85 ± 3.39
688.24	375.66 ± 3.20
672.84	347.23 ± 3.49
657.05	310.84 ± 2.79
640.87	278.94 ± 2.56
624.31	245.16 ± 2.36
607.39	222.48 ± 2.21
590.13	191.24 ± 1.99
572.54	170.21 ± 1.82
554.66	146.55 ± 1.65
536.48	117.30 ± 1.47
518.04	93.23 ± 1.29
499.37	71.75 ± 1.12
480.49	52.55 ± 0.97
461.39	38.51 ± 0.84
442.12	25.86 ± 0.73
422.71	16.14 ± 0.61
403.16	9.46 ± 0.52
383.50	5.56 ± 0.47
363.76	2.06 ± 0.41
343.95	1.04 ± 0.28
324.08	0.00 ± 0.11

7.2.4 $\pi^o\pi^o$ invariant mass E_γ= 400-500 MeV

M$_{\pi\pi}$ (MeV)	dσ/dM (nb/MeV)
265.00	0.00 ± 0.00
275.00	57.66 ± 4.44
285.00	83.61 ± 6.40
295.00	114.62 ± 8.26
305.00	94.66 ± 8.87
315.00	113.07 ± 9.61
325.00	78.32 ± 8.98
335.00	74.18 ± 8.49
345.00	87.18 ± 8.69
355.00	56.27 ± 7.63
365.00	46.26 ± 6.95
375.00	45.42 ± 6.60
385.00	32.25 ± 5.72
395.00	18.54 ± 4.80
405.00	10.25 ± 3.95
415.00	13.26 ± 3.51
425.00	6.26 ± 2.74
435.00	7.38 ± 2.44
445.00	-0.09 ± 1.43
455.00	1.58 ± 1.39
465.00	0.52 ± 0.98
475.00	1.50 ± 0.92
485.00	1.11 ± 0.70
495.00	0.00 ± 0.00

7.2.5 $\pi^o\pi^o$ invariant mass E_γ= 500-550 MeV

M$_{\pi\pi}$ (MeV)	dσ/dM (nb/MeV)
265.00	0.00 ± 0.00
275.00	109.51 ± 8.31
285.00	170.21 ± 13.56
295.00	157.19 ± 15.43
305.00	201.27 ± 18.38
315.00	203.43 ± 19.79
325.00	195.65 ± 19.96
335.00	220.75 ± 20.15
345.00	167.74 ± 18.42
355.00	157.62 ± 17.20
365.00	174.81 ± 17.02
375.00	132.26 ± 15.16
385.00	118.74 ± 14.29
395.00	108.07 ± 13.28
405.00	82.82 ± 11.75
415.00	62.75 ± 10.17
425.00	49.00 ± 8.86
435.00	50.32 ± 8.59
445.00	27.51 ± 6.64
455.00	15.03 ± 5.36
465.00	16.15 ± 5.27
475.00	0.20 ± 3.10
485.00	4.01 ± 3.10
495.00	0.98 ± 2.19

7.2.6 $\pi^o\pi^\pm$ invariant mass E_γ= 400-500 MeV

$M_{\pi\pi}$ (MeV)	dσ/dM (nb/MeV)
265.00	0.00 ± 0.00
275.00	122.72 ± 5.41
285.00	394.30 ± 11.30
295.00	399.08 ± 12.76
305.00	398.14 ± 13.15
315.00	371.41 ± 12.72
325.00	377.61 ± 12.47
335.00	359.16 ± 11.77
345.00	314.57 ± 10.72
355.00	248.26 ± 9.35
365.00	183.45 ± 7.79
375.00	130.46 ± 6.42
385.00	95.94 ± 5.35
395.00	65.72 ± 4.35
405.00	36.87 ± 3.36
415.00	29.59 ± 2.86
425.00	20.93 ± 2.31
435.00	11.33 ± 1.62
445.00	4.66 ± 1.00
455.00	2.37 ± 0.70
465.00	1.83 ± 0.53
475.00	0.82 ± 0.36
485.00	0.39 ± 0.29
495.00	0.69 ± 0.25

7.2.7 $\pi^o\pi^\pm$ invariant mass E_γ= 500-550 MeV

$M_{\pi\pi}$ (MeV)	dσ/dM (nb/MeV)
265.00	0.00 ± 0.00
275.00	206.87 ± 8.75
285.00	713.64 ± 20.08
295.00	881.57 ± 25.21
305.00	951.53 ± 28.23
315.00	951.14 ± 28.98
325.00	984.03 ± 29.28
335.00	987.31 ± 28.84
345.00	886.98 ± 26.80
355.00	838.41 ± 25.19
365.00	752.63 ± 23.05
375.00	600.54 ± 19.93
385.00	473.83 ± 17.16
395.00	378.94 ± 14.84
405.00	271.07 ± 12.24
415.00	209.61 ± 10.48
425.00	147.06 ± 8.62
435.00	112.21 ± 7.39
445.00	73.96 ± 5.92
455.00	54.47 ± 4.67
465.00	34.77 ± 3.24
475.00	17.60 ± 2.04
485.00	13.44 ± 1.59
495.00	6.70 ± 1.08

Chapter 8

Dictionary

Accidental coincidence: time coincidence of uncorrelated events. An event produced in the target may be related to an electron that is not the one that produced the incident photon. That can happen due to the large electron flux.

Background: event which is not of the studied reaction. It must be cut out during the analysis of this single event or sometimes must be subtracted if there is no way to kinematically distinguish it from a "good event".

BaF_2: material out of which are made the TAPS scintilators.

Barn: opposite of a surface. This unit is used for cross sections. 1 barn = 10^{-24} cm^{-2}.

^{40}Ca: nucleus of calcium of atomic number 40 (20 protons and 20 neutrons).

Calibration: convert any quantity into a physical one (energy, time).

CFD: electronic module used to know time of an electric signal.

Cluster: group of detectors measuring a signal produced by the same particle.

Coincidence: signal detected at very close time (within 1 or 2 ns for our experiments). Asking for coincidence is used to reject uncorrelated events. ie the 2 photons resulting from the decay of a pion that must be time coincident, or an electron detected in the tagger and a photon detected in TAPS must be coincident to know they are related.

Cross section: probability of an event of a given kind to happen. Expressed in $surface^{-1}$.

Delta (Δ): baryon of isospin I=3/2 (so existing in 4 charge states) which is the first resonance state in which a nucleon can be excited. The invariant mass of the Δ ground state is $M_\Delta = 1232$ MeV.

Differential cross section: decomposition of a total cross section in any variable (angle, mass of $\pi\pi$ pair in this work).

DLT: 30 Gb tapes on which the data are stored during the experiment.

Efficiency: probability for the experiment to reconstruct a given event produced in the target (depends on the detector type, geometry and the analysis used).

Electron tagger: cf tagger.

Eta meson (η): meson of isospin I=0 and mass M_η=547.3 MeV. Its main decay modes are 2γ at 39.43%, $3\pi^o$ at 32.51% and $\pi^o\pi^+\pi^-$ at 22.6%.

Four-vector: energy (E) and momentum $\vec{P}$ of a particle. The invariant mass of the particle is defined as the square of the four-vector which is E^2 - $\vec{P}^2$.

FSI: Final State Interactions. Any interactions from which suffer a particle produced in a nucleus before the particule can escape the nucleus and is detected.

FW wall: or forward wall; the larger TAPS wall of this setup. It is standing on the beam-line after the target (so in the forward direction).

GEANT: package written at CERN used for our simulations.

Incident photon: photon produced via bremsstrahlung in the radiator from a MAMI electron that induce an event in the calcium target.

Invariant mass: Lorentz-invariant quantity (it is the same in any frame) defined as the square of the four-momentum.

LED: electronic module used to know if an electric signal exceeds a given threshold.

MAMI: facility producing electrons of 882 MeV used for this experiment. It is located in Mainz (Germany).

Meson: hadron made of a quark and an antiquark (like π or η).

Missing mass: mass of what we don't detect. Used to check if an event is really of the identified kind.

Multiplicity: number of particles simultaneously detected. It can be for example the number of electrons detected in the tagger or the number of photons detected in TAPS.

N*: any excited I=1/2 state of the nucleon.

Photoproduction: exciting a nucleon with a real photon by opposition with electroproduction where the nucleon is excited by a virtual photon exchanged between an electron and the nucleon. The particles (usually mesons) emitted during the desexcitation of the nucleon are measured (like pion pairs in this work).

Pion: this meson made of quarks u and d is the lightest hadron. It has an ispospin I=1 so exist into 3 charge states. The π^o has a mass $M_{\pi^o} = 134.98$ MeV and decays at 98.8% into 2 photons with a mean life of $\tau = 8.4 \; . \; 10^{-17}$ s. The π^+ and π^- have a mass of $M_{\pi^\pm} = 139.57$ MeV and decay at 99.99 % into $\mu\nu$ in a mean time of 2.6 . 10^{-8} s.

Primary particle: particle detected in TAPS detectors by opposition with reconstructed particles which are not detected like π^o reconstructed in the analysis of the event with 2 photons (which are 2 primary particles).

Pulseshape: using the shape of the signal readout from the BaF_2detectors to discriminate between photons and other particles.

PSA: see pulseshape.

QDC: electronic module converting the analogic signal given by the photomultipliers of the BaF_2detectors into a digital signal proportional to the energy deposited by the particle.

Radiator: 4μm thick nickel foil standing in MAMI electron beam. Some of these electrons create bremsstrahlung photons in the forward direction which are used as a photon beam to excite calcium nuclei in the target.

Random background: combination of an event produced in the target with a wrong electron detected in the tagger. It is due to the high electron flux. For one photon interacting in the target, many uncorrelated photons fly through it. And for each of them an electron is detected in the tagger.

Scalers: count rate of the electrons in the tagger. Gives the number of photon that flew in the target when corrected with the tagging efficiency.

Simulation: producing fake random event looking like the data. Analyzing them the same way than the data allows to calculate detection efficiency as we know everything about the events that has been produced (which is not the case with real data).

Tagged photon: photon of which we know the energy thank to the electron tagger.

Tagger: the electron tagger is a device used to measure the energy of the electrons from which we can calculate the energy of the bremsstrahlung photon they just produced in the radiator.

Tagging efficiency: probability for a photon produced in the radiator to reach the target. Limited due to a collimator in the beam line to reduce the size of the beam at the target level.

TAPS: set of more than 500 BaF_2 photon detectors arranged for this work into 7 walls.

TDC: electronic module used to convert the BaF_2 signal into a time information.

TOF: time-of-flight. Time that takes a particle to fly from the target to the detectors. It depends on the energy and the mass of the particle. It is normalized to zero for a particle flying at the speed of light (photons).

Trigger: set of conditions that decides if an event that produced signals in the detectors is interessant enough for our subject of study to be recorded on tape to be latter fully analysed.

Veto: small plastic scintillators standing in front of each BaF_2 scintillator used to discriminate between charged and uncharged particles.

Acknowledgements

First of all, I would like to thank so much Bernd Krusche for his constant support, help and patience! (and untill the very last lines of this thesis and probably after too...).
I'm very grateful to Martin Kotulla for the huge progress I made since he came in Basel.
I would like to thank Su. Schadmand, J. Messchendorp, S. Janssen and M. Pfeiffer, for the priceless help they provided me on the analysis.
I wish to thank also the full TAPS collaboration, for the good time we spent in Mainz and Bonn and all I learnt with them, and especially Volker M., Reiner N., Dave H., David T., ...
I'm also grateful to I. Sick and J. Jourdan that did welcome me in the group.
I won't forget to thank all the people from the "82 Klingelberstrasse", from the group and outside. "Spéciale dédicace" to the office buddies and the french clique.
And a last and warm danke to Barbara and Astrid.
... et à la famille bien sûr!

Bibliography

[1] http://nobelprize.org/physics/laureates/2004/

[2] E. G. Drukarev and E. M. Levin, Prog. Paet. Nucl. Phys. **A556** (1991) 467.

[3] T. Hatsuda, Nucl. Phys. A544, 27 (1992).

[4] R. Brockmann and W. Weise, Phys. Lett. B367, 40 (1996).

[5] J. Goldstone, Nuovo Cim. 19 (1961) 154

[6] M. Gell-Mann, R.J. Oakes, and B. Renner, Phys. Rev. 175 (1968) 2195

[7] G.E. Brown, M. Rho, PRL 66 (1991) 2720

[8] M. Lutz, S. Klimt, W. Weise, Nucl. Phys. A542 (1992) 521

[9] P. Schuck et al., nucl-th/0002031

[10] V. Bernard et al., PRL 59 (1987) 966

[11] F. Bonutti et al., Phys. Rev. Lett. 77, 603 (1996)

[12] F. Bonutti et al., Phys. Rev. C60, 018201 (1999)

[13] F. Bonutti et al., Nucl. Phys. A677, 213 (2000)

[14] P. Camerini et al., Nucl. Phys. A 735 (2004) 89

[15] A. Starostin et al., Phys. Rev. Lett. 85 (2000) 5539

[16] J.G. Messchendorp et al., Phys. Rev. Lett. 89 (2002) 222302

[17] F. Bloch, Proceedings of the Hadron'03, X Intern. Conf. on Hadron Spectroscopy, Aschaffenburg, Germany, August 31 - September 6, 2003, AIP conference proceedings Vol. 717 (2004), p372

[18] B. Krusche and S. Schadmand, Progress in Particle and Nuclear Physics, 51 (2) (2003) 399

[19] B. Krusche et al., Phys. Rev. Lett. 74 (1995) 3736

[20] B. Krusche et al., Phys. Lett. B397 (1997) 171

[21] B. Krusche, to be published in Prog. Part. Nucl. Phys., nucl-ex/0411033

[22] B. Krusche et al., Eur. Phys. J. A22 (2004) 347

[23] B. Krusche et al., Eur. Phys. J. A22 (2004) 277

[24] Braghieri et al., Phys. Lett. B 363 (1995) 46

[25] Zabrodin et al., Phys. Rev. C 55 (1997) R1617

[26] Zabrodin et al., Phys. Rev. C 60 (1999) 055201

[27] V. Kleber et al., Eur. Phys. J. A 9 (2000) 1

[28] M. Wolf et al., Eur. Phys. J. A 9 (2000) 5

[29] F. Hrter, Phys. Lett. B401 (1997) 229

[30] J.A. Gomez Tejedor, E. Oset, Nucl. Phys. A 600 (1996) 413

[31] M. Post, S. Leupold, U. Mosel, Nucl. Phys. A 741, 81 (2004)

[32] W. Langgaertner et al., Phys. Rev. Lett. 87 (2001) 52001

[33] M. Hirata, K. Ochi, T. Takaki, Phys. Rev. Lett. 80, 5068 (1998)

[34] L.Y. Murphy, J.M. Laget, DAPHNIA/SPhN 96-10 (1996)

[35] L. Montanet et al., Phys. Rev. D50 (1994), Review of particle properties

[36] T. Frommhold et al., Phys. Lett. B295 (1992) 28-31

[37] T. Frommhold et al., Z. Phys. A350 (1994) 249-261

[38] N. Bianchi et al., Phys. Lett. B325 (1994) 333-336

[39] J.C. Nacher et al., Nucl. Phys. A695 (2001) 295-327

[40] Thomas Walcher, Prog. Part. Nucl. Phys. 24 (1990) 189

[41] J. Ahrens et al., Nuclear Physics News 4 (1994) 5-15

[42] I. Anthony et al., Nucl. Inst. and Meth. in Phys. Res. A301 (1991) 230-240

[43] S.J. Hall et al., Nucl. Inst. and Meth. in Phys. Res. A368 (1996) 698-708

[44] R. Novotny et al., IDEEE Trans. on Nucl. Science 38 (1991) 392

[45] M.J. Kotulla, Experimente zur Bestimmung des magnetischen Moments der Δ+(1232) Resonanz, PhD thesis, Giessen (Germany), 2001

[46] A.R. Gabler et al., Nucl. Instr. Meth. A346 (1994) 168-176

[47] T.C. Awes et al. Nucl. Inst. and Meth. in Phys. Res. A311 (1992) 130-138

[48] Kees Molenaar: Performance of TAPS in the Tagged Photon Beam of MAMI. 1992. Diploma work, Rijksuniversiteit Groningen (Nederland)

[49] PDG - Particle Data Group: Particle booklet. American institute of Physics, 1998

[50] PDG - Particle Data Group: Particle booklet. American institute of Physics, 2002

[51] Geant Detector Description and Simulation Tool. CERN Geneva, Switzerland, 1993

[52] F.James, Monte Carlo Phase Space, CERN 68-15, 1968

[53] S. Schadmand, private communication.

[54] J. Weiss et al., Eur. Phys. J. A16 (2003) 275

[55] P. Muehlich, private communication.

[56] P. Muehlich et al., Phys. Lett. B595 (2004) 216

[57] M. Effenberger, E.L. Bratkovskaya, U. Mosel, Phys. Rev. C60 (1999) 044614

[58] J. Lehr, L. Effenberger, U. Mosel, Nucl. Phys. A671 (2000) 503